mathematics

Article

Chaos of the Six-Dimensional Non-Autonomous System for the Circular Mesh Antenna

Ying Sun [1,*], Jingyi Liu [1], Junhua Zhang [2], Aiwen Wang [1] and Fei Mao [3]

[1] School of Applied Science, Beijing Information Science and Technology University, Beijing 100192, China
[2] College of Mechanical Engineering, Beijing Information Science and Technology University, Beijing 100192, China
[3] Beijing Zhongpuda Technology Company Ltd., Beijing 100015, China
* Correspondence: sunying0000@bistu.edu.cn

Abstract: In the process of aerospace service, circular mesh antennas generate large nonlinear vibrations under an alternating thermal load. In this paper, the Smale horseshoe and Shilnikov-type multi-pulse chaotic motions of the six-dimensional non-autonomous system for circular mesh antennas are first investigated. The Poincare map is generalized and applied to the six-dimensional non-autonomous system to analyze the existence of Smale horseshoe chaos. Based on the topological horseshoe theory, the three-dimensional solid torus structure is mapped into a logarithmic spiral structure, and the original structure appears to expand in two directions and contract in one direction. There exists chaos in the sense of a Smale horseshoe. The nonlinear equations of the circular mesh antenna under the conditions of the unperturbed and perturbed situations are analyzed, respectively. For the perturbation analysis of the six-dimensional non-autonomous system, the energy difference function is calculated. The transverse zero point of the energy difference function satisfies the non-degenerate conditions, which indicates that the system exists Shilnikov-type multi-pulse chaotic motions. In summary, the researches have verified the existence of chaotic motion in the six-dimensional non-autonomous system for the circular mesh antenna.

Keywords: circular mesh antenna; Smale horseshoe; the Poincare map; multi-pulse chaotic motion; the extended energy phase method

MSC: 34H10

check for updates

Citation: Sun, Y.; Liu, J.; Zhang, J.; Wang, A.; Mao, F. Chaos of the Six-Dimensional Non-Autonomous System for the Circular Mesh Antenna. *Mathematics* **2022**, *10*, 4454. https://doi.org/10.3390/math10234454

Academic Editor: Ivo Petráš

Received: 1 November 2022
Accepted: 23 November 2022
Published: 25 November 2022

1. Introduction

As an ideal form for large deployable structures, circular mesh antennas are applied to various aerospace missions, such as land sensing, earth observation, and deep space exploration. Circular mesh antennas are designed as a lightweight and flexible structure in orbit and use metal meshes as a reflecting surface [1–3]. The scale of the circular mesh antenna can reach the magnitude of 30–50 m, and it is difficult to understand and extract the essential nonlinear dynamic behaviors of the system from the mass data by the method of numerical simulations. Many scholars apply chaos theory to study the stability of a circular mesh antenna when it is deployed and locked in air service. By the nonlinear dynamics method, the chaotic phenomenon of the circular mesh antenna is predicted, and the validity and correctness of the prediction are verified by the theoretical and numerical simulations. Considering the complicated aerospace environment, the circular mesh antenna may cause large amplitude nonlinear vibrations [4]. This can seriously affect the accuracy and stability of the system. It is significant to study the nonlinear dynamical behavior of the circular mesh antenna system.

Nonlinear science has gradually developed into a frontier field of scientific research, and there is chaotic motion in nonlinear systems [5,6]. The researches of chaos have experienced the following stages of development: discovery, exploration, in-depth analysis and engineering applications. Originally, Smale et al. [7] constructed a map in the discrete dynamical system with shapes similar to horseshoes and represented chaos in a topological sense. Li and Yorke [8] gave the definition of chaos in the subsequent research. With the improvement and development discovery of chaos, modern chaos originated from Poincare's pioneering work [9,10] on homoclinic orbits generated by the transverse crossings of stable manifolds and unstable manifolds. In addition, many scholars and scientists have recently shown interest in applying these natural science models to social sciences [11] including areas such as psychology [12], family [13], addiction, happiness, and adult love and romantic relationships. Particularly, the relationship between love affairs [14] and romances of humans deal with different or similar contents in mathematics, biology and psychology. Deng et al. [15] proposed a new version of the nonlinear model with two women competing vehemently for an attractive man in a competitive love-triangle, which provides more insight into the dynamical behaviors of complex love-triangle relationships. Huang et al. describe a dynamical love model with the external environments of the love story of Romeo and Juliet with fuzzy membership function [16]. In the following analysis, the author used sinusoidal function as external environments which can represent the positive and negative characteristics of humans to analyze the chaotic behaviors in a novel extended love model [17]. The researchers reveal the mechanism of chaotic phenomena by the Lyapunov exponent, chaotic attractor, attractor basins [18], the Melnikov method [19] and other analytical methods. Zhang et al. [20] reported a class of two-dimensional rational memristive maps in which all attractors are hidden through numerical simulations. It is found that these maps can generate periodic, chaotic, quasi-periodic, and hyper-chaotic solutions. Wen et al. [21] studied the necessary conditions for a chaotic analytical solution of a Duffing oscillator with fractional order by the Melnikov method and investigated the bifurcation and chaos threshold of the system. Tian et al. analyzed the fundamental dynamics of the nonlinear systems with hidden attractors and line equilibria [22].

Among several types of chaotic motions, the horseshoes occur when the stable manifold and the unstable manifold cross transversely at a saddle fixed point. The horseshoes have been widely studied due to their special geometric structure. Huan et al. [23] put forward sufficient conditions for homoclinic orbits in the three-dimensional segmented affine systems and proved the existence of horseshoes under appropriate conditions. Li and Tomsovic [24] demonstrated that the behavior of unstable trajectories could be extended to linear combinations of homoclinic orbit in the Hamilton system. Furthermore, Shilnikov's theory and its extensions theories [25,26] show that the existence of homoclinic orbits or heteroclinic orbits implies the existence of horseshoes under certain conditions. At the same time, the Poincaré map is often utilized in the process of verifying horseshoes. Liu et al. [27] constructed the Poincaré map and applied integral manifold theory to study the conditions of periodic solution and the invariant torus for a four-dimensional nonlinear dynamical system.

There are mainly two different analytical methods for chaotic motion in high-dimensional nonlinear systems, the generalized Melnikov method [28,29] and the energy phase method [30]. The nonlinear dynamical behaviors of cantilever beams, thin plates, and functionally gradient frustoconical shells were studied using these two methods [31,32]. The Melnikov method was applied [33] to analyze the jump of multi-pulse chaotic dynamics. Moreover, the extended energy phase method [34] was used to study the chaotic motion of a four-dimensional nonlinear system. The higher-order Melnikov theories for time-period equations with homoclinic solutions were developed [35,36]. Yu et al. [37] applied the energy phase method on non-autonomous systems to study the energy dissipation of the system, and theoretically generalized the problem to 2n + 2 dimensions. Based on the energy phase method of Haller and Wiggins, Sun et al. [38] improved the energy phase method, studying the nonlinear dynamical behaviors of the circular mesh antennas. The geometry structure of three jumping pulses in six-dimensional phase space is described. For the choice of the two methods, the generalized Melnikov method is much more complicated than the energy phase method in terms of application, calculation and proof of expansion conditions. Therefore, the energy phase method is more suitable for solving complex nonlinear practical engineering problems.

Many studies of chaotic motions in physical and engineering systems may be related to homoclinic orbits. The researches on relevant properties of homoclinic orbits are important for chaotic motions. The properties near the homoclinic orbit are chaotic or transient chaotic phenomena that can be observed, which exist in physical systems. Chertovskih et al. [39] found 21 distinct nonlinear convective MHD attractors (13 steady states and 8 periodic regimes) and identified bifurcations in which they emerge. Cao et al. [40] present a novel construction of homoclinic/heteroclinic orbits in nonlinear oscillators. It is found that the present structure gives an accurate approximate solution of a homoclinic/heteroclinic orbit for large parametric value in relatively few harmonic terms. In the above research, the energy phase method had been extended to 2n + 2 dimensions in theory, and the multi-pulse chaotic motion of six-dimensional autonomous systems was analyzed in practical applications. The construction and description of differential manifolds for the six-dimensional nonlinear systems need further refined.

Due to the space environment, large deployable antennas will generate complex chaotic motions during the operation after unfolding and locking. In this paper, the chaotic motion of the six-dimensional non-autonomous system for the circular mesh antenna is studied. We analyze the horseshoes and multi-pulse chaotic motion of the six-dimensional non-autonomous system for circular mesh antenna. The Poincare map is applied to analyze the horseshoes in the six-dimensional non-autonomous system. The three-dimensional solid torus structures and in mutually vertical directions are selected, and the solid torus structure is mapped into a logarithmic spiral structure. Intercept the two-dimensional cross-section of the map, and the horseshoes occur. The perturbation analysis needs to be combined with the geometry structures of stable and unstable manifolds. Solving the dissipative energy difference function of the six-dimensional non-autonomous system, the transverse zeros and the upper bound of the dissipative factor are obtained. The energy difference function is verified to satisfy the non-degenerate conditions. The multi-pulse orbit jumped from the slow manifold returns to the domain of focus attraction.

2. Dynamical Equations and Simplifications

To study chaotic motions of the circular mesh antenna during the operation, according to reference [38], the three-degree-of-freedom ordinary differential equations are introduced as follows:

$$
\begin{aligned}
&\ddot{w}_1 + \mu_1 \dot{w}_1 + \omega_1^2 w_1 + f_1 \cos(\Omega t) w_1 + \alpha_{11} w_1^2 + \alpha_{12} w_2^2 + \alpha_{13} w_3^2 + \alpha_{14} w_1^3 + \alpha_{15} w_2^3 + \alpha_{16} w_3^3 \\
&+\alpha_{17} w_1 w_2 + \alpha_{18} w_2 w_3 + \alpha_{19} w_3 w_1 + \alpha_{20} w_1^2 w_2 + \alpha_{21} w_2^2 w_1 + \alpha_{22} w_2^2 w_3 + \alpha_{23} w_3^2 w_2 \\
&+\alpha_{24} w_1^2 w_3 + \alpha_{25} w_3^2 w_1 + \alpha_{26} w_1 w_2 w_3 = F_1 \cos(\Omega_1 t), \\
&\ddot{w}_2 + \mu_2 \dot{w}_2 + \omega_2^2 w_2 + f_2 \cos(\Omega t) w_2 + \beta_{11} w_1^2 + \beta_{12} w_2^2 + \beta_{13} w_3^2 + \beta_{14} w_1^3 + \beta_{15} w_2^3 + \beta_{16} w_3^3 \\
&+\beta_{17} w_1 w_2 + \beta_{18} w_2 w_3 + \beta_{19} w_3 w_1 + \beta_{20} w_1^2 w_2 + \beta_{21} w_2^2 w_1 + \beta_{22} w_2^2 w_3 + \beta_{23} w_3^2 w_2 \\
&+\beta_{24} w_1^2 w_3 + \beta_{25} w_3^2 w_1 + \beta_{26} w_1 w_2 w_3 = F_2 \cos(\Omega_2 t), \\
&\ddot{w}_3 + \mu_3 \dot{w}_3 + \omega_3^2 w_3 + f_3 \cos(\Omega t) w_3 + \gamma_{11} w_1^2 + \gamma_{12} w_2^2 + \gamma_{13} w_3^2 + \gamma_{14} w_1^3 + \gamma_{15} w_2^3 + \gamma_{16} w_3^3 \\
&+\gamma_{17} w_1 w_2 + \gamma_{18} w_2 w_3 + \gamma_{19} w_3 w_1 + \gamma_{20} w_1^2 w_2 + \gamma_{21} w_2^2 w_1 + \gamma_{22} w_2^2 w_3 + \gamma_{23} w_3^2 w_2 \\
&+\gamma_{24} w_1^2 w_3 + \gamma_{25} w_3^2 w_1 + \gamma_{26} w_1 w_2 w_3 = F_3 \cos(\Omega_3 t),
\end{aligned}
\tag{1}
$$

where w_1, w_2 and w_3 represent the amplitudes of the first, second, and third modes, μ_1, μ_2 and μ_3 stand for damping coefficient, while f_i and F_i represent the extrinsic excitation. Other coefficients in the equations are listed in reference [38]. Selecting the internal resonance relationship 1:4:6, and the six-dimensional average equations of the system are obtained.

$$\begin{aligned}\dot{x}_1 = &-\tfrac{1}{2}\mu_1 x_1 - (\sigma_1 + f_1)x_2 - \tfrac{9}{4}\alpha_{14}x_2\left(x_1^2 + x_2^2\right) \\ &-\tfrac{1}{2}\alpha_{21}x_2\left(x_3^2 + x_4^2\right) - \tfrac{1}{2}\alpha_{25}x_2\left(x_5^2 + x_6^2\right),\end{aligned} \tag{2}$$

$$\begin{aligned}\dot{x}_2 = &(\sigma_1 - f_1)x_1 - \tfrac{1}{2}\mu_1 x_2 + \tfrac{9}{4}\alpha_{14}x_1\left(x_1^2 + x_2^2\right) \\ &+\tfrac{1}{2}\alpha_{21}x_1\left(x_3^2 + x_4^2\right) + \tfrac{1}{2}\alpha_{25}x_1\left(x_5^2 + x_6^2\right),\end{aligned}$$

$$\begin{aligned}\dot{x}_3 = &-\tfrac{1}{2}\mu_2 x_3 - \tfrac{1}{4}\sigma_2 x_4 - \tfrac{9}{16}\beta_{15}x_4\left(x_3^2 + x_4^2\right) - \tfrac{1}{8}\beta_{20}x_4\left(x_1^2 + x_2^2\right) \\ &-\tfrac{1}{8}\beta_{23}x_4\left(x_5^2 + x_6^2\right) - \tfrac{1}{8}\beta_{24}x_1x_2x_5 - \tfrac{1}{16}\beta_{24}x_6\left(x_1^2 - x_2^2\right),\end{aligned}$$

$$\begin{aligned}\dot{x}_4 = &\tfrac{1}{4}\sigma_2 x_3 - \tfrac{1}{2}\mu_2 x_4 + \tfrac{9}{16}\beta_{15}x_3\left(x_3^2 + x_4^2\right) + \tfrac{1}{8}\beta_{20}x_3\left(x_1^2 + x_2^2\right) \\ &+\tfrac{1}{8}\beta_{23}x_3\left(x_5^2 + x_6^2\right) - \tfrac{1}{8}\beta_{24}x_1x_2x_6 + \tfrac{1}{16}\beta_{24}x_5\left(x_1^2 - x_2^2\right) - \tfrac{1}{4}F_2,\end{aligned}$$

$$\begin{aligned}\dot{x}_5 = &-\tfrac{1}{2}\mu_3 x_5 - \tfrac{1}{6}\sigma_3 x_6 - \tfrac{3}{8}\gamma_{16}x_6\left(x_5^2 + x_6^2\right) - \tfrac{1}{12}\gamma_{20}x_1x_2x_3 \\ &-\tfrac{1}{24}\gamma_{20}x_4\left(x_1^2 - x_2^2\right) - \tfrac{1}{12}\gamma_{22}x_6\left(x_3^2 + x_4^2\right) - \tfrac{1}{12}\gamma_{24}x_6\left(x_1^2 + x_2^2\right),\end{aligned}$$

$$\begin{aligned}\dot{x}_6 = &\tfrac{1}{6}\sigma_3 x_5 - \tfrac{1}{2}\mu_3 x_6 + \tfrac{3}{8}\gamma_{16}x_5\left(x_5^2 + x_6^2\right) - \tfrac{1}{12}\gamma_{20}x_1x_2x_4 \\ &+\tfrac{1}{24}\gamma_{20}x_3\left(x_1^2 + x_2^2\right) + \tfrac{1}{12}\gamma_{22}x_5\left(x_3^2 + x_4^2\right) + \tfrac{1}{12}\gamma_{24}x_5\left(x_1^2 + x_2^2\right) - \tfrac{1}{6}F_3,\end{aligned}$$

where σ_1, σ_2 and σ_3 are the perturbation parameters. The normative theory is used to simplify Equation (2), and its topological equivalent form is obtained. Equation (2) has an initial equilibrium solution $(x_1, x_2, x_3, x_4, x_5, x_6) = (0, 0, 0, 0, 0, 0)$. The Jacobi matrix of the linear part of Equation (2) is given by:

$$J = \begin{bmatrix} -\tfrac{1}{2}\mu_1 & -(\sigma_1 + f_1) & 0 & 0 & 0 & 0 \\ (\sigma_1 - f_1) & -\tfrac{1}{2}\mu_1 & 0 & 0 & 0 & 0 \\ 0 & 0 & -\tfrac{1}{2}\mu_2 & -\tfrac{1}{4}\sigma_2 & 0 & 0 \\ 0 & 0 & \tfrac{1}{4}\sigma_2 & -\tfrac{1}{2}\mu_2 & 0 & 0 \\ 0 & 0 & 0 & 0 & -\tfrac{1}{2}\mu_3 & -\tfrac{1}{6}\sigma_3 \\ 0 & 0 & 0 & 0 & \tfrac{1}{6}\sigma_3 & -\tfrac{1}{2}\mu_3 \end{bmatrix}. \tag{3}$$

The characteristic polynomial of the Jacobi matrix (3) is expressed as follows:

$$\begin{aligned} f(\lambda) = &\left(\lambda^2 + \lambda\mu_1 + \tfrac{1}{4}{\mu_1}^2 + {\sigma_1}^2 - {f_1}^2\right) \\ &\times\left(\lambda^2 + \lambda\mu_2 + \tfrac{1}{4}{\mu_2}^2 + \tfrac{1}{16}{\sigma_2}^2\right) \times \left(\lambda^2 + \lambda\mu_3 + \tfrac{1}{4}{\mu_3}^2 + \tfrac{1}{36}{\sigma_3}^2\right).\end{aligned} \tag{4}$$

When the conditions $\mu_1 = \mu_2 = \mu_3 = 0$ and ${\sigma_1}^2 - {f_1}^2 = 0$ are satisfied, the polynomial (4) has a pair of double-zero eigenvalues and two pairs of pure imaginary eigenvalues:

$$\lambda_{1,2} = 0, \lambda_{3,4} = \pm\frac{1}{4}\sigma_2 i, \lambda_{5,6} = \pm\frac{1}{6}\sigma_3 i. \tag{5}$$

The transformation matrix T is introduced as follows:

$$A = \begin{pmatrix} \lambda_1 & 0 & 0 & 0 & 0 & 0 \\ 0 & \lambda_2 & 0 & 0 & 0 & 0 \\ 0 & 0 & 0 & \frac{1}{4}\sigma_2 & 0 & 0 \\ 0 & 0 & -\frac{1}{4}\sigma_2 & 0 & 0 & 0 \\ 0 & 0 & 0 & 0 & 0 & \frac{1}{6}\sigma_3 \\ 0 & 0 & 0 & 0 & -\frac{1}{6}\sigma_3 & 0 \end{pmatrix} = T^{-1}JT. \tag{6}$$

According to the above transformation, the solution $x(t)$ of the linear part of Equation (2) can be expressed as follows:

$$x(t) = Te^{At}T^{-1}x_0 = T\begin{pmatrix} e^{\lambda_1 t} & 0 & 0 & 0 & 0 & 0 \\ 0 & e^{\lambda_2 t} & 0 & 0 & 0 & 0 \\ 0 & 0 & \cos\frac{1}{4}\sigma_2 t & \sin\frac{1}{4}\sigma_2 t & 0 & 0 \\ 0 & 0 & -\sin\frac{1}{4}\sigma_2 t & \cos\frac{1}{4}\sigma_2 t & 0 & 0 \\ 0 & 0 & 0 & 0 & \cos\frac{1}{6}\sigma_3 t & \sin\frac{1}{6}\sigma_3 t \\ 0 & 0 & 0 & 0 & -\sin\frac{1}{6}\sigma_3 t & \cos\frac{1}{6}\sigma_2 t \end{pmatrix}T^{-1}x_0. \tag{7}$$

When σ_2, $\sigma_3 < 0$, the geometric structure of the stable manifold and the unstable manifold of the six-dimensional non-autonomous system can be described. The unstable manifold E^u and the stable manifold E^s correspond to the pure imaginary eigenvalues and the real eigenvalues. The trajectory E^u is spirally rising out of the plane. Meanwhile E^s presents the shape of a homoclinic orbit on the plane $(u_1 - u_2)$, and converged near the saddle point P_1, as shown in Figure 1.

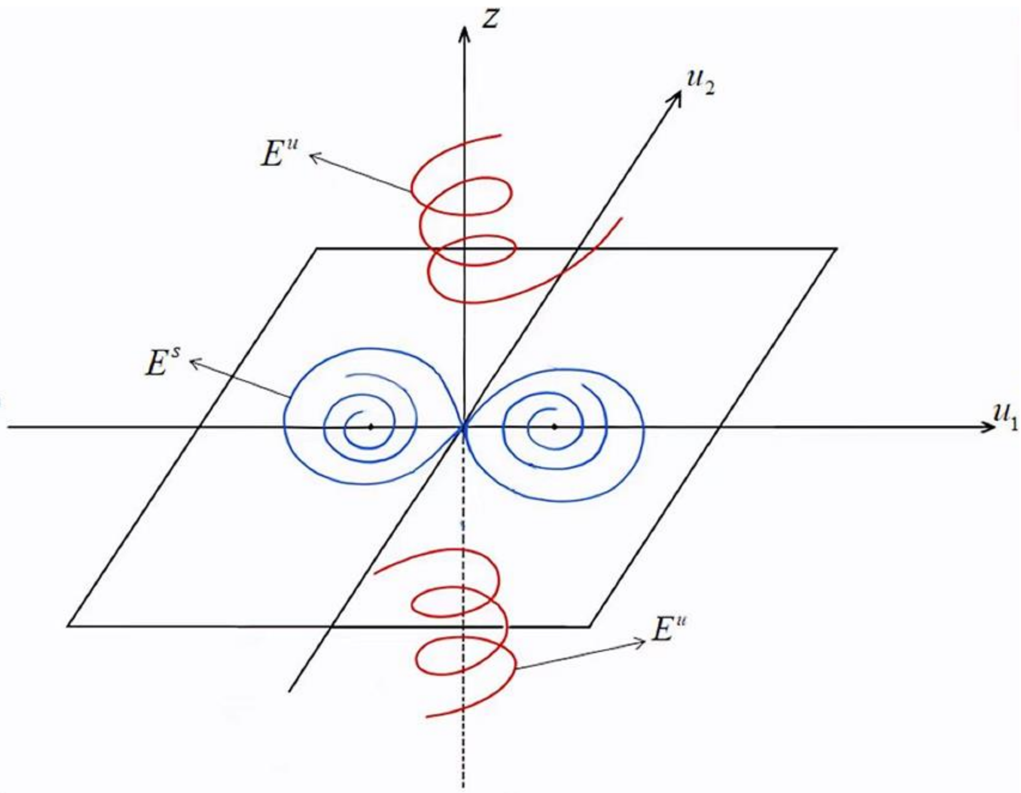

Figure 1. The geometric structures of stable and unstable manifolds.

After obtaining the manifold structure, let $f_1 = -1$, $\sigma_1 = f_1 + \overline{\sigma}_1$, μ_1, μ_2, μ_3, $\overline{\sigma}_1$, F_2 and F_3 are perturbation parameters. The third-order normal form with parameters for Equation (2) is given by:

$$\begin{aligned}
\dot{y}_1 &= -\tfrac{1}{2}\mu_1 y_1 + (1-\overline{\sigma}_1) y_2 \\
\dot{y}_2 &= \overline{\sigma}_1 y_1 - \tfrac{1}{2}\mu_1 y_2 + \tfrac{9}{4}\alpha_{14} {y_1}^3 + \tfrac{1}{2}\alpha_{21} y_1 {y_3}^2, \\
&+ \tfrac{1}{2}\alpha_{21} y_1 {y_4}^2 + \tfrac{1}{2}\alpha_{25} y_1 {y_5}^2 + \tfrac{1}{2}\alpha_{25} y_1 {y_6}^2 \\
\dot{y}_3 &= -\tfrac{1}{2}\mu_2 y_3 - \tfrac{1}{4}\sigma_2 y_4 + \tfrac{9}{128}\beta_{15} {y_3}^3 - \tfrac{63}{128}\beta_{15} {y_4}^3 \\
&- \tfrac{1}{8}\beta_{20} {y_1}^2 y_4 - \tfrac{63}{128}\beta_{15} {y_3}^2 y_4 + \tfrac{9}{128}\beta_{15} y_3 {y_4}^2 + \tfrac{1}{16}\beta_{23} y_3 {y_5}^2, \\
&- \tfrac{1}{16}\beta_{23} y_4 {y_5}^2 + \tfrac{1}{16}\beta_{23} y_3 {y_6}^2 - \tfrac{1}{16}\beta_{23} y_4 {y_6}^2 \\
\dot{y}_4 &= \tfrac{1}{4}\sigma_2 y_3 - \tfrac{1}{2}\mu_2 y_4 + \tfrac{63}{128}\beta_{15} {y_3}^3 + \tfrac{9}{128}\beta_{15} {y_4}^3 \\
&+ \tfrac{1}{8}\beta_{20} {y_1}^2 y_3 + \tfrac{9}{128}\beta_{15} {y_3}^2 y_4 + \tfrac{63}{128}\beta_{15} y_3 {y_4}^2 + \tfrac{1}{16}\beta_{23} y_3 {y_5}^2, \\
&+ \tfrac{1}{16}\beta_{23} y_4 {y_5}^2 + \tfrac{1}{16}\beta_{23} y_3 {y_6}^2 + \tfrac{1}{16}\beta_{23} y_4 {y_6}^2 - \tfrac{1}{4}F_2 \\
\dot{y}_5 &= -\tfrac{1}{2}\mu_3 y_5 - \tfrac{1}{6}\sigma_3 y_6 - \tfrac{21}{64}\gamma_{16} {y_6}^3 - \tfrac{1}{12}\gamma_{24} {y_1}^2 y_6, \\
&- \tfrac{1}{12}\gamma_{22} {y_3}^2 y_6 - \tfrac{1}{12}\gamma_{22} {y_4}^2 y_6 - \tfrac{21}{64}\gamma_{16} {y_5}^2 y_6 \\
\dot{y}_6 &= \tfrac{1}{6}\sigma_3 y_5 - \tfrac{1}{2}\mu_3 y_6 + \tfrac{21}{64}\gamma_{16} {y_5}^3 + \tfrac{1}{12}\gamma_{24} {y_1}^2 y_5, \\
&+ \tfrac{1}{12}\gamma_{22} {y_3}^2 y_5 + \tfrac{1}{12}\gamma_{22} {y_4}^2 y_5 + \tfrac{21}{64}\gamma_{16} y_5 {y_6}^2 - \tfrac{1}{6}F_3.
\end{aligned} \tag{8}$$

Let

$$y_3 = I_1 \cos\theta_1, y_4 = I_1 \sin\theta_1, y_5 = I_2 \cos\theta_2, y_6 = I_2 \sin\theta_2. \tag{9}$$

Substituting the transformation (9) into Equation (8), the system (8) in the polar coordinates is rewritten as follows:

$$\begin{aligned}
\dot{y}_1 &= -\frac{1}{2}\mu_1 y_1 + (1-\overline{\sigma}_1) y_2, \\
\dot{y}_2 &= \overline{\sigma}_1 y_1 - \frac{1}{2}\mu_1 y_2 + \frac{9}{4}\alpha_{14} {y_1}^3 + \frac{1}{2}\alpha_{21} y_1 {I_1}^2 + \frac{1}{2}\alpha_{25} y_1 {I_2}^2, \\
\dot{I}_1 &= -\frac{1}{2}\mu_2 I_1 - \frac{1}{4}F_2 \sin\theta_1, \\
I_1\dot{\theta}_1 &= \frac{1}{4}\sigma_2 I_1 + \frac{63}{128}\beta_{15} {I_1}^3 - \frac{1}{8}\beta_{20} {y_1}^2 I_1 + \frac{1}{16}\beta_{23} I_1 {I_2}^2 - \frac{1}{4}F_2 \cos\theta_1, \\
\dot{I}_2 &= -\frac{1}{2}\mu_3 I_2 - \frac{1}{6}F_3 \sin\theta_2, \\
I_2\dot{\theta}_2 &= \frac{1}{6}\sigma_3 I_2 + \frac{21}{64}\gamma_{16} {I_2}^3 + \frac{1}{12}\gamma_{24} {y_1}^2 I_2 + \frac{1}{12}\gamma_{22} {I_1}^2 I_2 - \frac{1}{6}F_3 \cos\theta_2.
\end{aligned} \tag{10}$$

Equation (10) is rewritten as the simple normal form:

$$\begin{aligned}
\dot{u}_1 &= c_1 u_2, \\
\dot{u}_2 &= -c_2 u_1 - \mu_1 u_2 + c_3 {u_1}^3 + c_4 u_1 {I_1}^2 + c_5 u_1 {I_2}^2, \\
\dot{I}_1 &= c_6 I_1 - \frac{1}{4}F_2 \sin\theta_1, \\
I_1\dot{\theta}_1 &= c_7 I_1 + c_8 {I_1}^3 + c_9 {u_1}^2 I_1 + c_{10} I_1 {I_2}^2 - \frac{1}{4}F_2 \cos\theta_1,
\end{aligned} \tag{11}$$

$$\dot{I}_2 = c_{11} I_2 - \frac{1}{6} F_3 \sin \theta_2,$$

$$I_2 \dot{\theta}_2 = c_{12} I_2 + c_{13} {I_2}^3 + c_5 {u_1}^2 I_2 + c_{10} {I_1}^2 I_2 - \frac{1}{6} F_3 \cos \theta_2.$$

Among them, $c_1 = \frac{\gamma_{25}}{\alpha_{25}}$, $c_2 = \frac{\alpha_{25}}{4\gamma_{25}}[1 - 4\overline{\sigma}_1(1-\overline{\sigma}_1)]$, $c_3 = -\frac{9\alpha_{14}{\alpha_{25}}^3}{4{\gamma_{25}}^3}(1-\overline{\sigma}_1)^2$, $c_4 = \frac{\alpha_{21}\alpha_{25}}{2\gamma_{25}}(1-\overline{\sigma}_1)$, $c_5 = \frac{{\alpha_{25}}^2}{2\gamma_{25}}(1-\overline{\sigma}_1)$, $c_6 = -\frac{1}{2}\mu_2$, $c_7 = \frac{1}{4}\sigma_2$, $c_8 = \frac{63}{128}\beta_{15}$, $c_9 = \frac{1}{8}\beta_{20}\frac{{\alpha_{25}}^2}{\gamma_{25}}(1-\overline{\sigma}_1)$, $c_{10} = \frac{1}{16}\beta_{23}$, $c_{11} = -\frac{1}{2}\mu_3$, $c_{12} = \frac{1}{6}\sigma_3$, $c_{13} = \frac{21}{64}\gamma_{16}$.

To analyze the influence of damping coefficient and thermal excitation on the nonlinear dynamic behavior of the system, the perturbation parameters of damping coefficient and thermal excitation are introduced as follows:

$$\mu_1 \to \varepsilon\mu_1\,,\ \mu_2 \to \varepsilon\mu_2\,,\ \mu_3 \to \varepsilon\mu_3\,,\ F_2 \to \varepsilon F_2\,,\ F_3 \to \varepsilon F_3. \tag{12}$$

Equation (11) is rewritten as the Hamilton system with disturbance terms, and the system is extended to a non-autonomous system. The multi-scale method is used to introduce the time differential form:

$$\dot{u}_1 = \frac{\partial H}{\partial u_2} + \varepsilon g^{u_1} = c_1 u_2, \tag{13}$$

$$\dot{u}_2 = -\frac{\partial H}{\partial u_1} + \varepsilon g^{u_2} = -c_2 u_1 + c_3 {u_1}^3 + c_4 u_1 {I_1}^2 + c_5 u_1 {I_2}^2 - \varepsilon\mu_1 u_2,$$

$$\dot{I}_1 = \frac{\partial H}{\partial \theta_1} + \varepsilon g^{I_1} = \varepsilon c_6 I_1 - \frac{1}{4}\varepsilon F_2 \sin\theta_1,$$

$$I_1\dot{\theta}_1 = -\frac{\partial H}{\partial I_1} + \varepsilon g^{\theta_1} = c_7 I_1 + c_8 {I_1}^3 + c_9 {u_1}^2 I_1 + c_{10} I_1 {I_2}^2 - \frac{1}{4}\varepsilon F_2 \cos\theta_1,$$

$$\dot{I}_2 = \frac{\partial H}{\partial \theta_2} + \varepsilon g^{I_2} = \varepsilon c_{11} I_2 - \frac{1}{6}\varepsilon F_3 \sin\theta_2,$$

$$I_2\dot{\theta}_2 = -\frac{\partial H}{\partial I_2} + \varepsilon g^{\theta_2} = c_{12} I_2 + c_{13} {I_2}^3 + c_5 {u_1}^2 I_2 + c_{10} {I_1}^2 I_2 - \frac{1}{6}\varepsilon F_3 \cos\theta_2,$$

$$\dot{\phi} = \omega_1.$$

When $\varepsilon = 0$, the Hamilton function of the unperturbed system from Equation (13) is

$$\begin{aligned} H = {} & \tfrac{1}{2}c_1 + \tfrac{1}{2}c_2{u_1}^2 - \tfrac{1}{4}c_3{u_1}^4 - \tfrac{1}{2}\left(c_4{I_1}^2 + c_5{I_2}^2\right){u_1}^2 - \tfrac{1}{2}c_7{I_1}^2 \\ & - \tfrac{1}{4}c_8{I_1}^4 - \tfrac{1}{2}c_{10}{I_1}^2{I_2}^2 - \tfrac{1}{2}c_{12}{I_2}^2 - \tfrac{1}{4}c_{13}{I_2}^4. \end{aligned} \tag{14}$$

When $\varepsilon \neq 0$, the system is a perturbed system, each disturbance term can be expressed as:

$$g^{u_1} = 0, g^{u_2} = -\mu_1 u_2, \tag{15}$$

$$g^{\theta_1} = -\frac{1}{4}F_2\cos\theta_1, g^{\theta_2} = -\frac{1}{6}F_3\cos\theta_2,$$

$$g^{I_1} = c_6 I_1 - \frac{1}{4}F_2\sin\theta_1, g^{I_2} = c_{11} I_2 - \frac{1}{6}F_3\sin\theta_2.$$

3. Smale Horseshoe

In the six-dimensional non-autonomous dynamic system, there are chaotic motions in the system which can be judged through the geometric structure near the homoclinic orbits.

Based on the Poincare map method given by reference [41], it is promoted and applied to analyze the horseshoes in the six-dimensional non-autonomous system. Due to the large amount of calculation and the difficulty in constructing the topological structure, the unperturbed system is decoupled into the first two-dimensional system (u_1, u_2) and the latter four-dimensional system $(I_1, \theta_1, I_2, \theta_2)$. Consider the first two-dimensional equations.

When $\varepsilon = 0$, the remaining variables satisfy the conditions $\dot{I}_1 = 0$ and $\dot{I}_2 = 0$. Consider Equation (13) as follows:

$$\dot{u}_1 = c_1 u_2, \tag{16}$$

$$\dot{u}_2 = -c_2 u_1 + c_3 {u_1}^3 + c_4 u_1 {I_1}^2 + c_5 u_1 {I_2}^2.$$

The Hamilton function of Equation (16) can be expressed as:

$$H_1 = \frac{1}{2} c_1 {u_2}^2 + \frac{1}{2} c_2 {u_1}^2 - \frac{1}{4} c_3 {u_1}^4 - \frac{1}{2}\left(c_4 {I_1}^2 + c_5 {I_2}^2\right) {u_1}^2. \tag{17}$$

Considering the system parameters, when $c_3 c_1 < 0$, it is found that the system had homoclinic bifurcation. Let $c_3 > 0$ and $c_1 < 0$, discuss the characteristics of homoclinic bifurcation based on the above parameter settings. When the condition $c_2 - c_4 I_1^2 - c_5 I_2^2 < 0$ is satisfied, Equation (16) has a unique zero solution $(u_1, u_2) = (0, 0)$ which is a saddle point. When $c_2 - c_4 I_1^2 - c_5 I_2^2 > 0$, Equation (16) has three singular points. The phase diagram near the equilibrium point, responding to both of the two cases, is plotted in Figure 2. The eigenvalues obtained from the first two-dimensional system are expressed as $\lambda = \pm\sqrt{-(c_2 - c_4 I_1^2 - c_5 I_2^2)}$, when the system parameters are taken as $c_1 = -1.1$, $c_2 = 5.4$, $c_3 = 4.795$, $c_4 = -1.9$, $c_5 = 6$, $I_1 = 0.98$, $I_2 = 0.49$, the phase diagram is shown in Figure 2a, while the system parameters are chosen as $c_1 = -1.1$, $c_2 = -5.4$, $c_3 = 4.795$, $c_4 = -1.9$, $c_5 = 6$, $I_1 = 0.98$, $I_2 = 0.49$, and the phase diagram is plotted in Figure 2b. The initial value is selected as $x_0 = [0.98, -1.001]$.

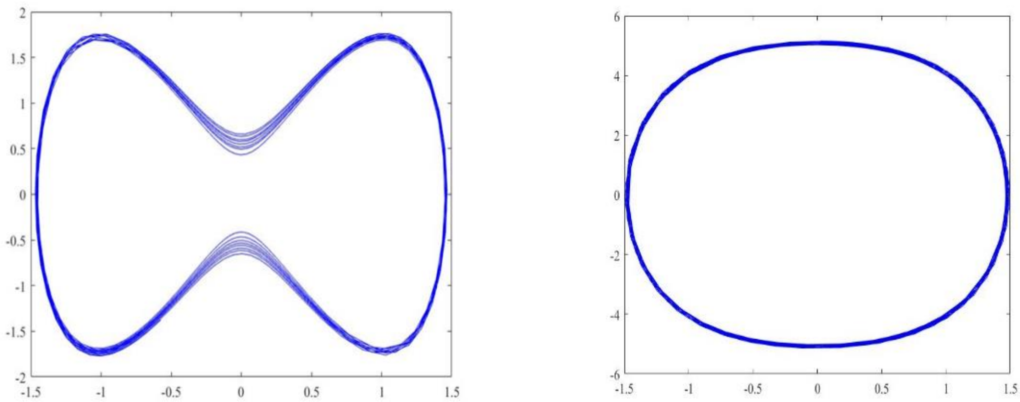

(**a**) (**b**)

Figure 2. The phase diagram of the plane $(u_1 - u_2)$ (**a**) The phase diagram of the plane $(u_1 - u_2)$ under condition $c_2 - c_4 I_1^2 - c_5 I_2^2 > 0$; (**b**) The phase diagram of the plane $(u_1 - u_2)$ under condition $c_2 - c_4 I_1^2 - c_5 I_2^2 < 0$.

To study the orbit properties of the first two-dimensional system (u_1, u_2) better, we rewrite Equation (16) into the following form:

$$\dot{u}_1 = c_1 u_2 + f_1(u_1, u_2, I), \tag{18}$$

$$\dot{u}_2 = -c_2 u_1 + f_2(u_1, u_2, I).$$

Among them, $(u_1, u_2, I) \in R^1 \times R^1 \times R^1$, f_1, f_2=$O(|x|^2 + |y|^2)$, I is a parameter and $c_1 \cdot c_2 < 0$. We make the following assumptions on Equation (18).

A1: $c_1 \cdot c_2 < 0$. (A1 is local nature, which concerns the properties of the eigenvalues of the vector field linearized about the fixed point.)

A2: At $I = 0$, Equation (18) possesses a homoclinic orbit connecting the hyperbolic fixed point $P_1(u_1, u_2) = (0, 0)$ and itself. On both sides of $I = 0$, the homoclinic orbit breaks in a transverse way. The stable and unstable manifolds have different orientations on both sides of $I = 0$. (A2 is global in nature. It supposes the existence of a homoclinic orbit.)

When the parameters of the model satisfy the above two assumptions, it is found that the stable manifold lies outside of the unstable manifold when $I > 0$. The stable manifold and the unstable manifold overlap when $I = 0$. When $I < 0$, the stable manifold lies inside of the unstable manifold. The above description is shown in Figure 3.

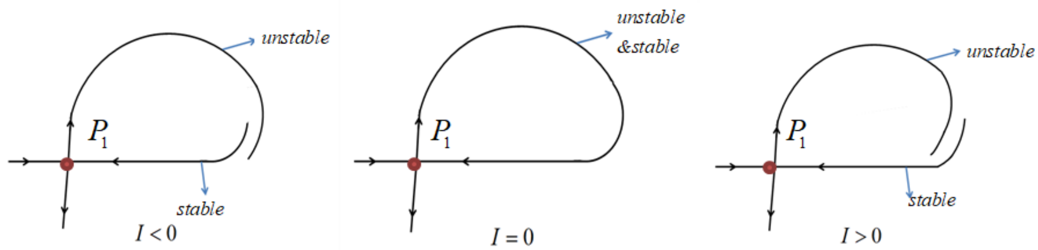

Figure 3. The homoclinic orbit local properties.

To analyze the properties near the homoclinic orbit, it is necessary to compute a Poincare map near the homoclinic orbit. Set up the domains for the Poincare map. The planes Π_0 and Π_1 of the small neighborhoods in two vertical directions near the equilibrium point are introduced as follows:

$$\Pi_0 = \{(u_1, u_2) \in C_\varepsilon^s | u_1 = \varepsilon > 0, u_2 > 0\}, \tag{19}$$

$$\Pi_1 = \{(u_1, u_2) \in C_\varepsilon^u | u_1 > 0, u_2 = \varepsilon > 0\}.$$

The geometric structure of Π_0 and Π_1 under the situation $I = 0$ is given in Figure 4. From Figure 4, the map P_0^L is mapped from Π_0 to Π_1. The flow is defined by the linearization of the system about the origin point, which is expressed as $u_1(t) = u_{10} \cdot e^{c_1 t}$, $u_2(t) = u_{20} \cdot e^{-c_2 t}$. There is a point $(\varepsilon, u_{20}) \in \Pi_0$ to reach Π_1 under the action of Equation (18) given by solving $\varepsilon = u_{20} \cdot e^{-c_2 t}$. Both u_{10} and u_{20} are the initial values. The map P_0^L is denoted by:

$$P_0^L : \Pi_0 \to \Pi_1, (\varepsilon, u_{20}) \mapsto (\varepsilon \cdot (\frac{\varepsilon}{u_{20}})^{\frac{c_1}{c_2}}, \varepsilon). \tag{20}$$

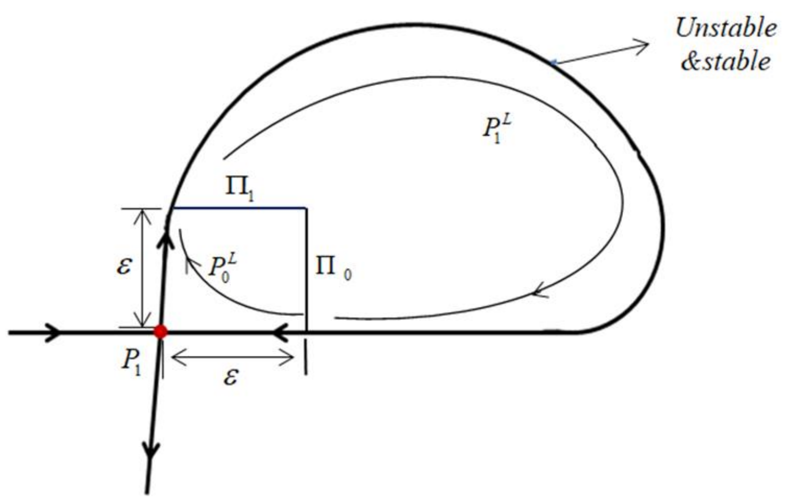

Figure 4. When $I = 0$, the plane Π_0 and Π_1 under the two-dimensional Poincare map.

Define a map P_1^L from plane Π_1 to Π_0. Since the map from plane Π_1 to Π_0 takes only finite time, there exists a subspace $U \subset \Pi_1$ in Π_1 satisfied the equation

$$P_1(u_1, u_2, I) = (P_{11}(u_1, u_2, I), P_{12}(u_1, u_2, I)) : U \subset \Pi_1 \to \Pi_0, \tag{21}$$

$$P_1^L : \Pi_1 \to \Pi_0, (u_1, \varepsilon) \mapsto (\varepsilon, c_1 u_1 - c_2 I).$$

The Poincare map is denoted by:

$$P^L = P_1^L \circ P_0^L : V \subset \Pi_0 \to \Pi_1, (\varepsilon, u_{20}) \mapsto (\varepsilon, c_1 \varepsilon (\frac{\varepsilon}{u_{20}})^{\frac{c_1}{c_2}} - c_2 I), \tag{22}$$

$$V = (P_0^L)^{-1}(U), P^L(u_2, I) : u_2 \mapsto A u_2^{|\frac{c_1}{c_2}|} - c_2 I.$$

where $A = c_1 \varepsilon^{1+\frac{c_1}{c_2}} > 0$.

The fixed point of the Poincare map is essential for discussing the positional relationship between the fixed point and the periodic orbit. To solve the fixed point of the Poincare map, the fixed points can be displayed graphically as the intersection of the graph of $P^L(u_2, I)$ with the line $P^L(u_2, I) = A u_2^{|\frac{c_1}{c_2}|} - c_2 I = u_2$ for different values of I. The discussion is categorized by the term $\frac{c_1}{c_2}$. There are two cases:

Case 1: When $|c_1| > |c_2|$. For this case, $D_{u_2} P^L(0, 0) = 0$. According to different values of I, the graph of $(P^L - u_2)$ appears as shown in Figure 5 for $I < 0$, $I = 0$ and $I > 0$.

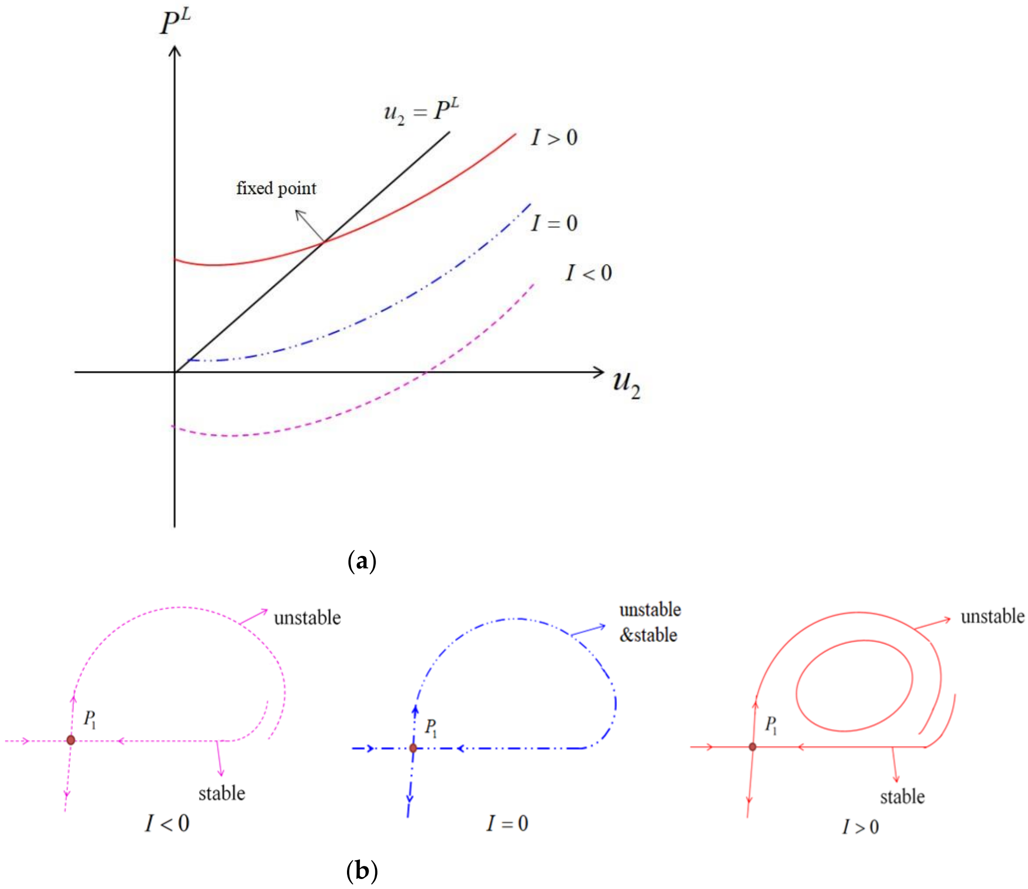

Figure 5. The positional relationship when $\frac{c_1}{c_2} > 1$, (**a**) The fixed point diagram. (**b**) The position relationship between the fixed point and periodic orbit.

In Figure 5a, when the equation $P^L(u_2, I) = A u_2^{|\frac{c_1}{c_2}|} - c_2 I = u_2$ is satisfied, the graph has an intersection point for $I > 0$, it is the fixed point in case 1. The fixed point is stable and hyperbolic, since $0 < D_{u_2}P^L < 1$ for I sufficiently small. From the topological structure in Figure 5b, it is concluded that the fixed point corresponds to an attracting periodic orbit of Equation (18). The fixed point would occur for $I < 0$, while the homoclinic orbit breaks.

Case 2: When $|c_1| < |c_2|$. For this case, $D_{u_2}P^L(0,0) \to \infty$. According to the different values of I, the graph $(P^L - u_2)$ is described as shown in Figure 6 for $I < 0$, $I = 0$ and $I > 0$.

Figure 6a shows that when the equation $P^L(u_2, I) = Au_2^{|\frac{c_1}{c_2}|} - c_2 I = u_2$ is satisfied, the fixed point appears at $I < 0$. It is a repelling fixed point. In Figure 6b, when corresponding to $I < 0$, this fixed point tends to repel the periodic orbits. The fixed point would occur for $I > 0$, while the homoclinic orbit breaks.

We are considering the Poincare map in the system $(I_1, \theta_1, I_2, \theta_2)$. Horseshoes are one of the most critical characteristics of chaotic phenomena in nonlinear dynamical behaviors. Intercepting the linear flow of Equation (2), equations are rewritten into the following form:

$$\dot{x}_1 = -\frac{1}{2}\mu_1 x_1 - (\sigma_1 + f_1)x_2 + P(x_1, x_2, x_3, x_4, x_5, x_6), \tag{23}$$

$$\begin{aligned}
\dot{x}_2 &= (\sigma_1 - f_1)x_1 - \frac{1}{2}\mu_1 x_2 + Q(x_1, x_2, x_3, x_4, x_5, x_6), \\
\dot{x}_3 &= -\frac{1}{2}\mu_2 x_3 - \frac{1}{4}\sigma_2 x_4 + R(x_1, x_2, x_3, x_4, x_5, x_6), \\
\dot{x}_4 &= \frac{1}{4}\sigma_2 x_3 - \frac{1}{2}\mu_2 x_4 + S(x_1, x_2, x_3, x_4, x_5, x_6), \\
\dot{x}_5 &= -\frac{1}{2}\mu_3 x_5 - \frac{1}{6}\sigma_3 x_6 + T(x_1, x_2, x_3, x_4, x_5, x_6), \\
\dot{x}_6 &= \frac{1}{6}\sigma_3 x_5 - \frac{1}{2}\mu_3 x_6 + U(x_1, x_2, x_3, x_4, x_5, x_6),
\end{aligned}$$

Under the initial condition of $(x_1, x_2, x_3, x_4, x_5, x_6) \in R^6$, μ_1, μ_2, μ_3, σ_2, $\sigma_3 > 0$ and $\sigma_1 - f_1 > 0$. The functions of P, Q, R, S, T, U all belong to the space C^2. $(x_1, x_2, x_3, x_4, x_5, x_6) = (0, 0, 0, 0, 0, 0)$ is a fixed point of Equation (23), and the eigenvalues of Equation (23) linearized about the origin are given by $\lambda_{1,2} = 0$, $\lambda_{3,4} = \pm\frac{1}{4}\sigma_2 i$,. $\lambda_{5,6} = \pm\frac{1}{6}\sigma_3 i$. We make two assumptions for the above system, such as:

(H1). Equation (23) has homoclinic orbits connecting the fixed point $(0, 0, 0, 0, 0, 0)$ to it.

(H2). μ_1, μ_2 and μ_3 are different from each other.

Equation (23) has a pair of double-zero eigenvalues and two pairs of pure imaginary eigenvalues. The map P_2^L near the origin point is derived from the linearized flow. It is more suitable to use the polar coordinates. The following transformations are introduced:

$$\dot{x}_3 = r_1 \cos\theta_1,\ \dot{x}_4 = r_1 \sin\theta_1,\ \dot{x}_5 = r_2 \cos\theta_2, \dot{x}_6 = r_2 \cos\theta_2. \tag{24}$$

The linearized vector fields are given by:

$$\dot{r}_1 = -\frac{1}{2}\mu_2 r_1,\ \dot{\theta}_1 = \frac{1}{4}\sigma_2,\ \dot{r}_2 = -\frac{1}{2}\mu_3 r_2,\ \dot{\theta}_2 = \frac{1}{6}\sigma_3. \tag{25}$$

The linear flow represented by Equation (25) can be rewritten in a new form as follows:

$$r_1(t) = r_{10}e^{-\frac{1}{2}\mu_2 t},\ \theta_1(t) = \frac{1}{4}\sigma_2 t + \theta_{10},\ r_1(t) = r_{20}e^{-\frac{1}{2}\mu_3 t},\ \theta_2(t) = \frac{1}{6}\sigma_3 t + \theta_{20}. \tag{26}$$

where r_{10}, r_{20}, θ_{10}, θ_{20} are the initial values.

The three-dimensional solid torus structures Π_2 and Π_3 of the vector field near the origin point are introduced as follows:

$$\Pi_2 = \{(r_1, \theta_1, r_2, \theta_2) | r_1 = \varepsilon\}, \tag{27}$$

$$\Pi_3 = \{(r_1, \theta_1, r_2, \theta_2) | r_2 = \varepsilon\},$$

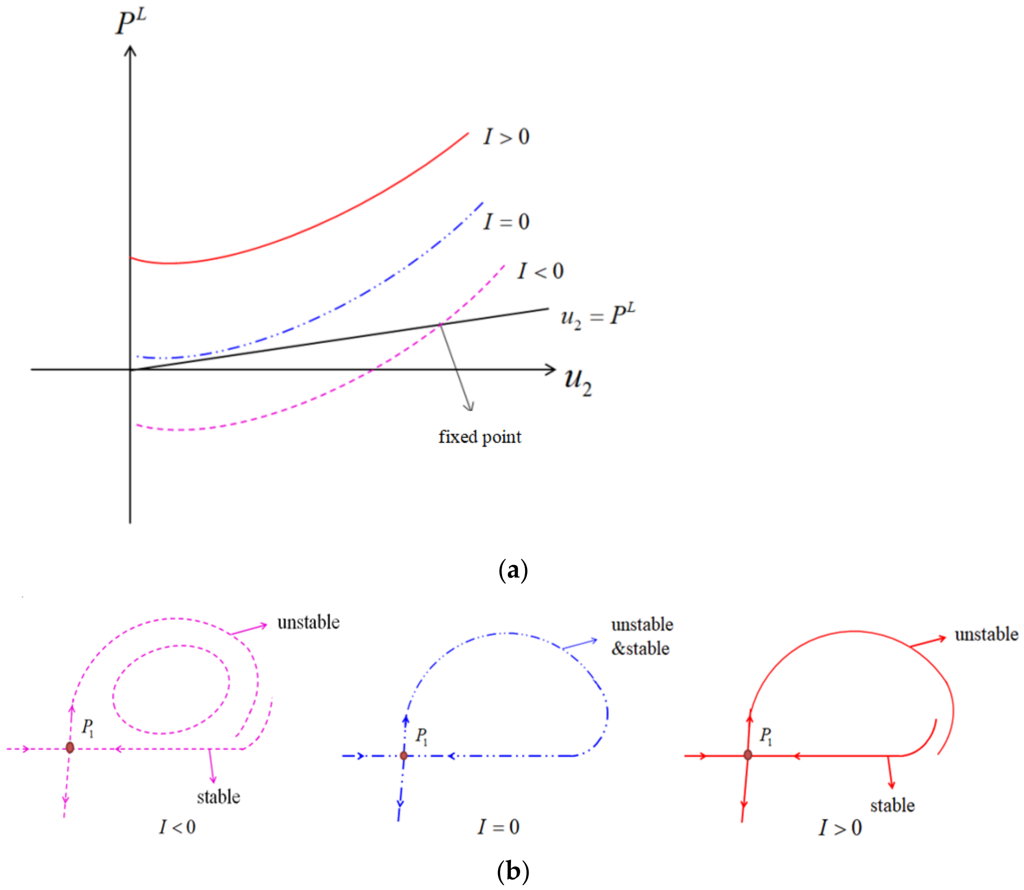

Figure 6. The positional relationship when $\frac{c_1}{c_2} < 1$, (**a**) The fixed-point diagram. (**b**) The Positional relationship between fixed point and periodic orbit.

It is found that Π_2 and Π_3 are all three-dimensional solid torus structures which are highly symmetrical. The central circle of Π_2 and the locally unstable manifold intersect at $r_2 = 0$. The central circle of Π_3 intersect with the stable manifold at $r_1 = 0$. The intersections of locally stable manifolds and unstable manifolds with homoclinic manifolds are defined as p_0 and $p_1.p_0 = (\varepsilon, \overline{\theta}, 0, 0) = \Gamma \cap W^s_{loc}$, $p_1 = (0, 0, \varepsilon, \overline{\theta}) = \Gamma \cap W^u_{loc}$. The geometry structure of the solid torus structures and manifolds is depicted as shown in Figure 7.

Figure 7a represents a cross-section diagram taken from two three-dimensional solid torus structure diagrams. Figure 7b describes the process of the P^L_2 map in the three-dimensional solid torus structures Π_2 and Π_3, respectively. Let $\varepsilon = r_{20} e^{\frac{1}{2}\mu_3 t}$, the time $t = 2\mu_3 \log^{\frac{\varepsilon}{r_{20}}}$ mapped is obtained from Π_2 to Π_3. The map P^L_2 is denoted as

$$P^L_2 : \Pi_2 \mapsto \Pi_3, \begin{pmatrix} \varepsilon \\ \theta_1 \\ r_2 \\ \theta_2 \end{pmatrix} \to \begin{pmatrix} \varepsilon\left(\frac{r_2}{\varepsilon}\right)^{\frac{\mu_2}{\mu_3}} \\ \theta_1 + \frac{\sigma_2}{2\mu_3} \log^{\frac{\varepsilon}{r_2}} \\ \varepsilon \\ \theta_2 - \frac{\sigma_3}{3\mu_3} \log^{\frac{\varepsilon}{r_2}} \end{pmatrix}. \tag{28}$$

Consider an infinite sequence of solid annuli contained in Π_2:

$$A_k = \left\{ (r_1, \theta_1, r_2, \theta_2) | r_1 = \varepsilon, \overline{\theta}_1 - \alpha \leq \theta_1 \leq \overline{\theta}_1 + \alpha, \varepsilon e^{\frac{-2\pi(k+1)\mu_3}{\sigma_2}} \leq r_2 \leq \varepsilon e^{\frac{-2\pi k \mu_3}{\sigma_2}}, 0 \leq \theta_2 \leq 2\pi \right\}. \tag{29}$$

For $\forall \alpha > 0, k = 0, 1, 2 \ldots$, the geometry structure is shown in Figure 8.

The behavior of boundary of A_k under Π_2 needs to be investigated. The boundary of A_k consists of the union of terminal linear structures at both ends, and also consists of a left terminal and a right terminal which are expressed as E_k^l and E_k^r. Its inner and outer surfaces are marked as S_k^i and S_k^o. The above terminal structures are denoted by:

$$E_k^l = \left\{(r_1, \theta_1, r_2, \theta_2) | r_1 = \varepsilon, \theta_1 = \overline{\theta}_1 - \alpha, \varepsilon e^{(k+1)c} \le r_2 \le \varepsilon e^{kc}, 0 \le \theta_2 \le 2\pi\right\}, \tag{30}$$

$$E_k^r = \left\{(r_1, \theta_1, r_2, \theta_2) | r_1 = \varepsilon, \theta_1 = \overline{\theta}_1 + \alpha, \varepsilon e^{(k+1)c} \le r_2 \le \varepsilon e^{kc}, 0 \le \theta_2 \le 2\pi\right\},$$

$$S_k^i = \left\{(r_1, \theta_1, r_2, \theta_2) | r_1 = \varepsilon, \overline{\theta}_1 - \alpha \le \theta_1 \le \overline{\theta}_1 + \alpha, r_2 = \varepsilon e^{(k+1)c}, 0 \le \theta_2 \le 2\pi\right\},$$

$$S_k^o = \left\{(r_1, \theta_1, r_2, \theta_2) | r_1 = \varepsilon, \overline{\theta}_1 - \alpha \le \theta_1 \le \overline{\theta}_1 + \alpha, r_2 = \varepsilon e^{kc}, 0 \le \theta_2 \le 2\pi\right\},$$

where $c = \frac{-4\pi\mu_3}{\sigma_2}$. The geometry boundary structure is shown in Figure 9. The geometry structure was regarded as a solid torus structure nested in a three-dimensional ring structure in a small neighborhood α of θ_1. The structure includes left terminal, right terminal, inner surface and outer surface. Substituting Equation (30) into the map P_2^L, the following forms are obtained.

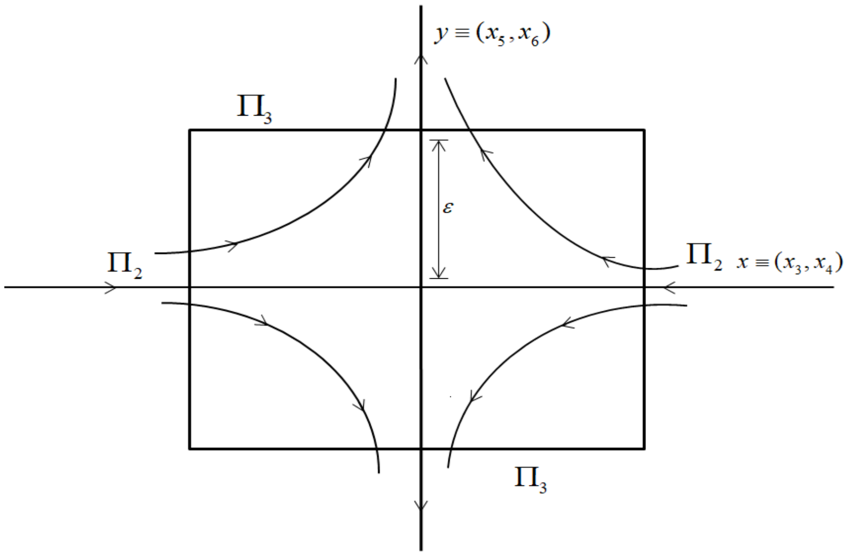

(**a**)

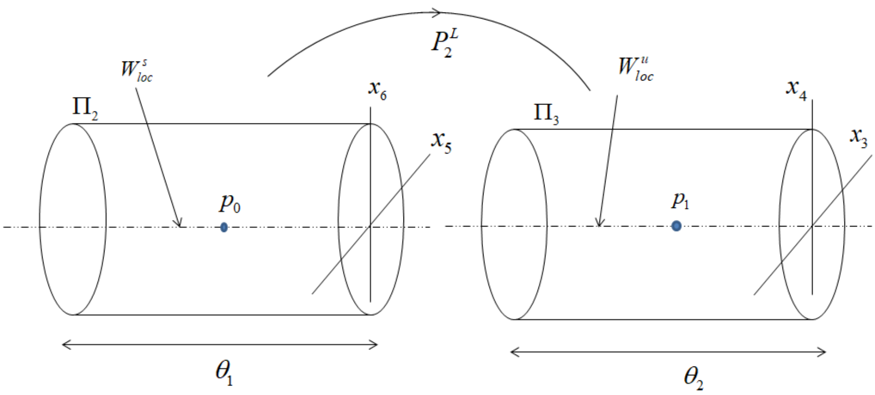

(**b**)

Figure 7. The three-dimensional solid torus structure and cross section of Π_2 and Π_3. (**a**) The cross section of Π_2 and Π_3. (**b**) The three-dimensional solid torus structure of Poincare map P_2^L.

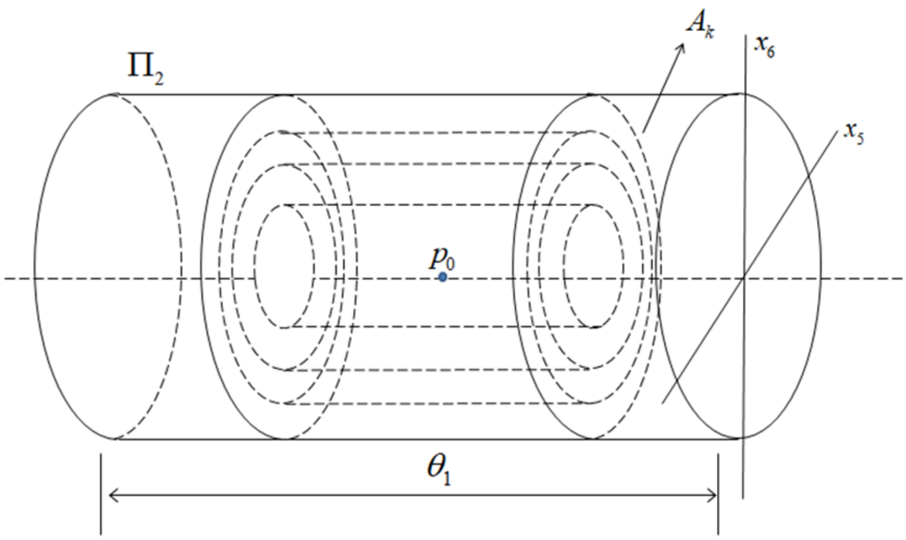

Figure 8. The three-dimensional torus structure Π_2 and the nested solid ring structure.

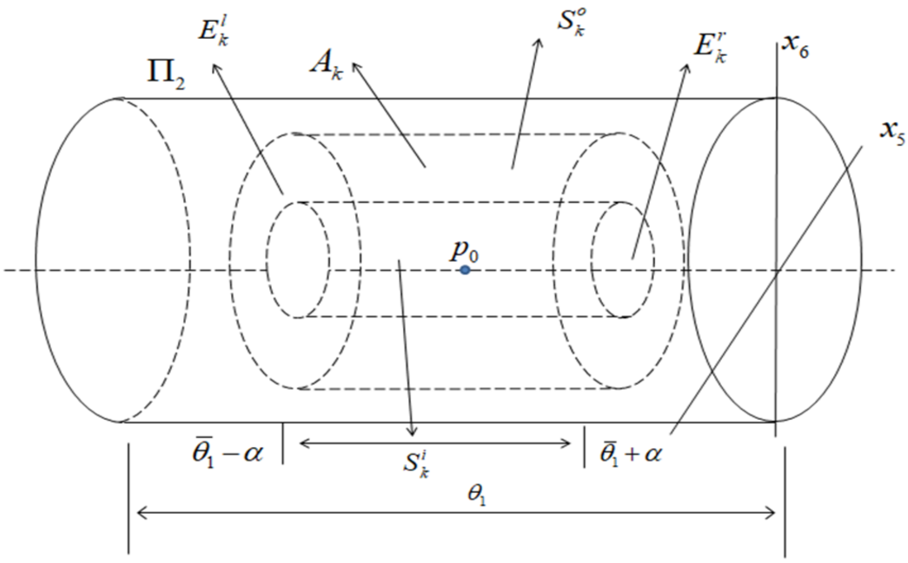

Figure 9. The three-dimensional torus structure Π_2 and the boundary descriptions.

$$P_2^L(E_k^l) = \left\{ (r_1, \theta_1, r_2, \theta_2) \middle| \begin{array}{l} \varepsilon e^{\frac{-2\pi(k+1)\mu_2}{\sigma_2}} \le r_1 \le \varepsilon e^{\frac{-2\pi k\mu_2}{\sigma_2}}, r_2 = \varepsilon, 0 \le \theta_1 \le 2\pi, \\ \bar{\theta}_1 - \alpha + 2\pi k \le \theta_1 \le \bar{\theta}_1 - \alpha + 2\pi(k+1) \end{array} \right\}, \tag{31}$$

$$P_2^L(E_k^r) = \left\{ (r_1, \theta_1, r_2, \theta_2) \middle| \begin{array}{l} \varepsilon e^{\frac{-2\pi(k+1)\mu_2}{\sigma_2}} \le r_1 \le \varepsilon e^{\frac{-2\pi k\mu_2}{\sigma_2}}, r_2 = \varepsilon, 0 \le \theta_1 \le 2\pi, \\ \bar{\theta}_1 + \alpha + 2\pi k \le \theta_1 \le \bar{\theta}_1 + \alpha + 2\pi(k+1) \end{array} \right\},$$

$$P_2^L(S_k^i) = \left\{ (r_1, \theta_1, r_2, \theta_2) \middle| \begin{array}{l} r_1 = \varepsilon e^{\frac{-2\pi(k+1)\mu_2}{\sigma_2}}, r_2 = \varepsilon, 0 \le \theta_1 \le 2\pi, \\ \bar{\theta}_1 - \alpha + 2\pi(k+1) \le \theta_1 \le \bar{\theta}_1 + \alpha + 2\pi(k+1) \end{array} \right\},$$

$$P_2^L(E_k^l) = \left\{ (r_1, \theta_1, r_2, \theta_2) \middle| \begin{array}{l} r_1 = \varepsilon e^{\frac{-2\pi k\mu_2}{\sigma_2}}, r_2 = \varepsilon, 0 \le \theta_1 \le 2\pi, \\ \bar{\theta}_1 - \alpha + 2\pi k \le \theta_1 \le \bar{\theta}_1 + \alpha + 2\pi k \end{array} \right\},$$

Each terminal structure under the Poincare map P_2^L is given, the geometric structure was constructed in Figure 10, as a solid ring nested inside the three-dimensional torus structure. Similarly, stable manifold and unstable manifold can be distinguished. The cross-section under the Poincare map is given in Figure 10b. For sufficiently large k,$P^L(A_k)$ cuts through A_k. For $\mu_3 > \mu_2$, P^L expands along the μ_3 direction. When $\mu_3 < \mu_2$, P^L contracts along the μ_3 direction. Lines parallel to W^s_{loc} are contracted. Lines connecting S^i_k and S^o_k are stretched under P^L. From the above analysis, P^L contains two expanding directions and one contracting direction if $\mu_3 > \mu_2$, or one expanding direction and two contracting directions when $\mu_3 < \mu_2$. It follows that P^L contains horseshoes and the accompanying chaos phenomena.

The change process of the cross-section is regarded as the behavior of introducing a vertical line and horizontal sum line on the two-dimensional plane. The four lines can be mapped into a logarithmic spiral structure through the transformation of the Poincare map, as shown in Figure 11.

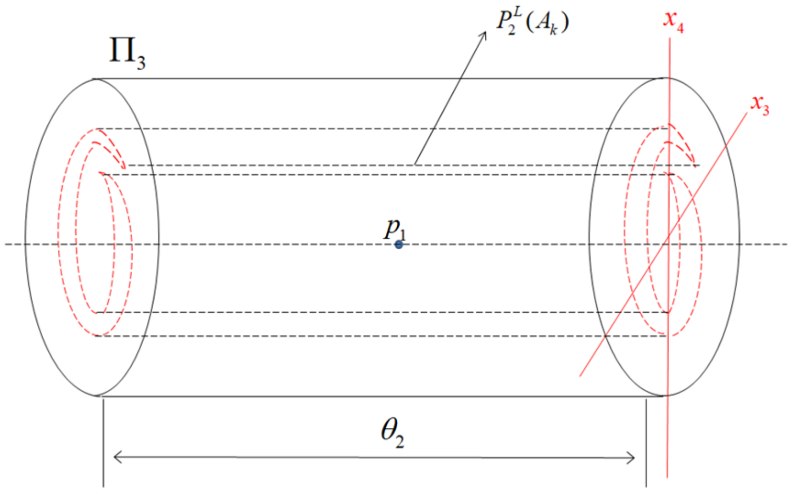

(**a**)

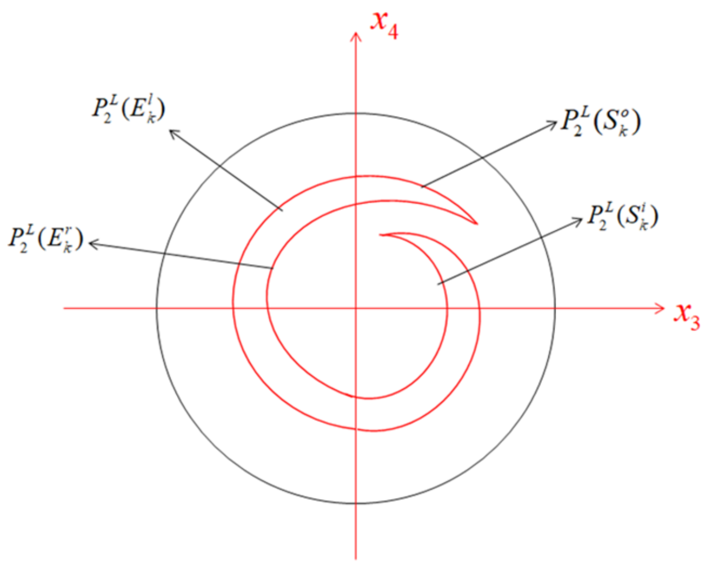

(**b**)

Figure 10. The geometric structure of the Poincare map. (**a**) The Poincare map of three-dimensional structure. (**b**) The cross-section of the logarithmic spiral map.

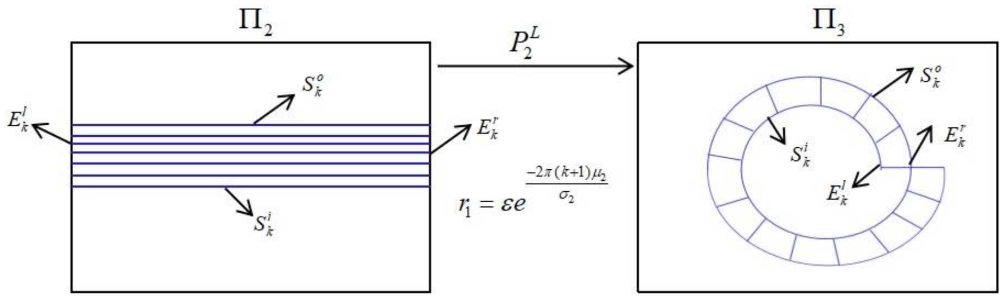

Figure 11. The process of from a planar linear structure to a logarithmic spiral structure.

In the three-dimensional space, the structure of the Poincare map $P^L(A_k)$ goes through A_k, as is shown in Figure 12. By Theorem 3.2.17 in reference [34], the Poincare map $P^L(A_k)$ satisfies the conditions that the logarithmic spiral structure after the Poincare map has two intersections with the upper and lower boundaries of the rectangular area. It is verified that within the six-dimensional non-autonomous system exist horseshoes.

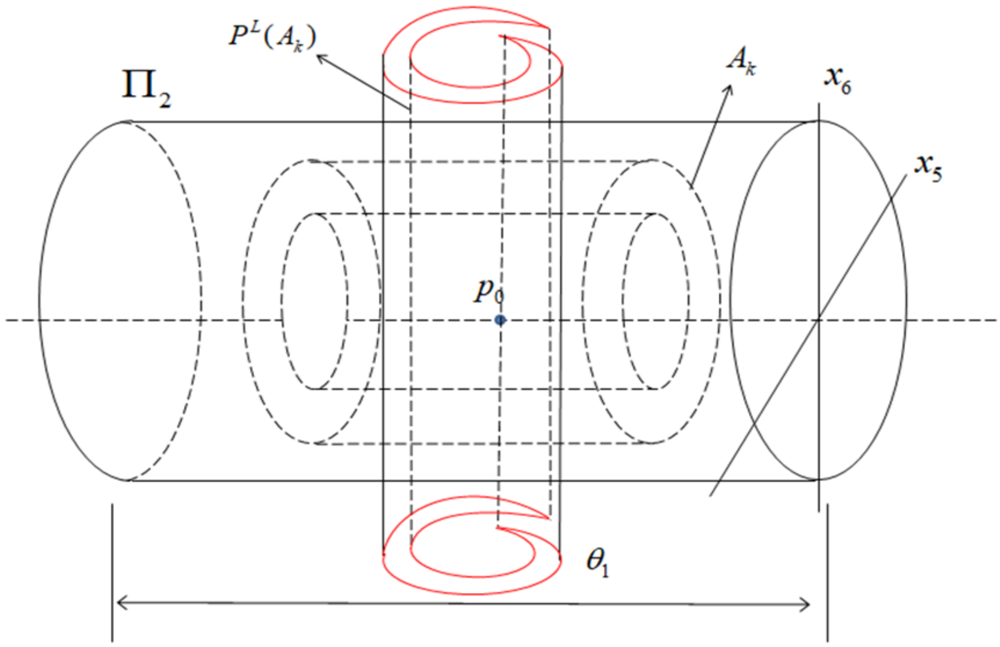

Figure 12. The four-dimensional Poincare map.

4. Shilnikov-Type Multi-Pulse Chaotic Motions

The nonlinear dynamical characteristics of the unperturbed and perturbed system of Equation (13) are given, respectively. Based on the eigenvalues calculated in Equation (5), the homoclinic bifurcation exists in the system (16) when $c_1 \cdot c_3 < 0$. Let $c_3 > 0$ and $c_1 < 0$, the equilibrium point is obtained; discuss the parameter settings as follows:

1. When $c_2 - c_4 {I_1}^2 - c_5 {I_2}^2 < 0$, the system has one equilibrium point $P(u_1, u_2) = (0, 0)$, which is a saddle point.
2. When $c_2 - c_4 {I_1}^2 - c_5 {I_2}^2 > 0$, the system has three singular points, which are $P_1(0,0)$ and $P_{2,3} = (\pm B, 0)$. When $c_2 - c_4 {I_1}^2 - c_5 {I_2}^2 = 0$, the system is in a critical state and bifurcates. The saddle point $P(u_1, u_2) = (0, 0)$ bifurcates into three solutions $P_1(0,0)$ and $P_{2,3} = (\pm B, 0)$, and the pitchfork bifurcation appears. $P_1(0,0)$ is saddle point and $P_{2,3} = (\pm B, 0)$ are center points, where $B = \left\{ \frac{1}{c_3} [c_2 - c_4 I_1^2 - c_5 I_2^2] \right\}^{\frac{1}{2}}$.

Substituting $P_{2,3}$ into the Hamilton function (17), the expression of the homoclinic orbit is given by:

$$u_1(T_1) = \pm\sqrt{\frac{2\varepsilon_1}{c_3}}\operatorname{sech}(2\sqrt{c_1\varepsilon_1}T_1), \tag{32}$$

$$u_2(T_1) = \pm 2\varepsilon_1\sqrt{\frac{2}{c_1c_3}}\tan(2\sqrt{c_1\varepsilon_1}T_1)\sec\mathrm{h}(2\sqrt{c_1\varepsilon_1}T_1),$$

Discuss the latter four-dimensional system, the variables I_1, I_2, θ_1 and θ_2 represent the amplitude and the phase, respectively. When $I_\mathrm{i} \geq 0, i = (1,2)$, the system has two center points $P_{2,3} = (\pm B, 0)$ and a saddle point $P_1(0,0)$ under the unperturbed case. A pair of homoclinic orbits $u^h_{\pm i}(T_1, I_i), i = (1,2)$ exist in the interval $I \in (I_1, I_2) \notin [I_{11}, I_{12}] \times [I_{21}, I_{22}] \subset R^2$. The homoclinic orbits satisfy the condition $\lim\limits_{T\to\pm\infty_1} u_{\pm i}(T_1, I_i) = P_{2,3}$, which T_1 is defined as a two-dimensional slowly varying manifold in the phase space. In the six-dimensional non-autonomous phase space, the five-dimensional hyperbolic invariant manifold M_0 is defined as follows:

$$M_0 = \left\{(u, I, \theta) \in R \times R^2 \times S^2 | u = P_1, I_1 < I < I_2, 0 \leq \theta_i < 2\pi\right\}, i = (1,2). \tag{33}$$

M_0 has five-dimensional stable manifold $W^s(M_0)$ and five-dimensional unstable manifold $W^u(M_0)$. The singular point connected by the homoclinic orbit Γ along $W^s(M_0)$ and $W^u(M_0)$. The homoclinic orbit Γ converges to the saddle point $P_1(0,0)$. $W^s(M_0)$ and $W^u(M_0)$ intersect transversely along a five-dimensional homoclinic manifold. The homoclinic orbit Γ is defined as follows:

$$\begin{aligned}\Gamma = \Big\{(u, I, \theta)\Big| u = u^h_{\pm i}(T_1, I_i), I \in (I_1, I_2),\\ \gamma = \textstyle\int_0^{T_1} D_{I_i}H\left(u^h_{\pm i}(T_1, I_i), I\right)ds + \theta_{i0}\Big\}, i = (1,2).\end{aligned} \tag{34}$$

Two-dimensional regular hyperbolic invariant rings $\theta(I)$ corresponding to each amplitude of vibrations have a three-dimensional stable manifold $W^s(\theta(I))$ and unstable manifold $W^s(\theta(I))$, respectively. The θ represents the phase of vibration. It is consistent with the formation of a three-dimensional homoclinic manifold.

According to the criterion of boundary manifold, the five-dimensional unstable manifold at the boundary is inflow manifold. It is a local characteristic of the six-dimensional non-autonomous system.

Constraining the unperturbed system (12) to the invariant manifold, the latter four-dimensional equations are rewritten as:

$$\begin{gathered}\dot{I}_1 = 0, \\ I_1\dot{\theta}_1 = c_7I_1 + c_8{I_1}^3 + c_9{u_1}^2I_1 + c_{10}I_1{I_2}^2, \\ \dot{I}_2 = 0, \\ I_2\dot{\theta}_2 = c_{12}I_2 + c_{13}{I_2}^3 + c_5{u_1}^2I_2 + c_{10}{I_1}^2I_2, \\ \dot{\phi} = \omega_1.\end{gathered} \tag{35}$$

$I \in (I_1, I_2) = C$, where C is the constant. Based on the condition in reference [30], when the conditions $D_{I_i}H(q_\pm(I)\,,\ I) \neq 0, i = (1,2)$ are satisfied, the solution of the system (35) is a two-dimensional ring. When $D_{I_i}H(q_\pm(I)\,,\ I) = 0, i = (1,2)$, the solution is a fixed point, $D_{I_i}H(q_\pm(I)\,,\ I), i = (1,2)$ are denoted as:

$$D_{I_1}H(P_{2,3}\,,\ I_r) = c_7 I_{1r} + c_8 {I_{1r}}^3 + c_9 {P_{2,3}}^2 I_{1r} + c_{10} I_{1r} {I_{2r}}^2, \tag{36}$$

$$D_{I_2}H(P_{2,3}\,,\ I_r) = c_{12} I_{2r} + c_{13} {I_{2r}}^3 + c_5 {P_{2,3}}^2 I_{2r} + c_{10} {I_{1r}}^2 I_{2r}.$$

The system (35) generates resonance under conditions (36). I_{1r} and I_{2r} represent the resonance values, which are expressed as follows:

$${I_{1r}}^2 = \frac{c_3(c_{10}c_{12} - c_7c_{13}) + \varepsilon_1(c_5c_{10} - c_9c_{13})}{c_3(c_8c_{13} - {c_{10}}^2)}, \tag{37}$$

$${I_{2r}}^2 = \frac{c_3(c_8c_{12} - c_7c_{10}) + \varepsilon_1(c_5c_8 - c_9c_{10})}{c_3({c_{10}}^2 - c_8c_{13})},$$

Substituting the homoclinic orbit equations into Equation (35), the vibration phases θ_1 and θ_2 are obtained as:

$$\theta_1 = \left(d_1 + \frac{2\varepsilon_1 c_9}{c_3}\right)T_1 - \frac{c_9\sqrt{\varepsilon_1}}{c_3\sqrt{c_1}}\tanh(2\sqrt{c_1\varepsilon_1}T_1) + \theta_{10}, \tag{38}$$

$$\theta_2 = \left(d_2 + \frac{2\varepsilon_1 c_9}{c_3}\right)T_1 - \frac{c_5\sqrt{\varepsilon_1}}{c_3\sqrt{c_1}}\tanh(2\sqrt{c_1\varepsilon_1}T_1) + \theta_{20}.$$

When $d_1 = c_7 + c_8{I_1}^2 + c_{10}{I_2}^2$, $d_2 = c_{12} + c_{10}{I_1}^2 + c_{13}{I_2}^2$, θ_{10} and θ_{20} are initial values of the vibration phases. The phase shifts are denoted as:

$$\Delta\theta_i = \theta(+\infty\,,\ I_i) - \theta(-\infty\,,\ I_i), i = (1,2), \tag{39}$$

$$\Delta\theta_1 = \frac{2c_9\sqrt{\varepsilon_1}}{c_3\sqrt{c_1}}, \Delta\theta_2 = \frac{2c_5\sqrt{\varepsilon_1}}{c_3\sqrt{c_1}}.$$

The six-dimensional non-autonomous system with perturbation is investigated. The invariant manifold M_0 becomes the invariant manifold M_ε, when the system is subjected to dissipative perturbations. Due to the saddle point P_1 keep the hyperbolic characteristics under dissipative perturbations, M_ε is sufficiently close to M_0. A section $\Sigma^{\phi_0} = \{(u_1, u_2, I_1, I_2, \theta, \phi)|\phi = \phi_0\}$ is introduced into the system. The hyperbolic invariance of the subspace M_0, $W^s(M_0)$ and $W^u(M_0)$ still keep the properties. The invariant manifold of the combined cross-section can be expressed as the following forms:

$${M_0}^{\phi_0} = \{(u_1, u_2, I_1, I_2, \theta)|(u_1, u_2) = P_1, I_{i1} < I < I_{i2}, 0 \leq \theta_i \leq 2\pi\}, \tag{40}$$

$${M_\varepsilon}^{\phi} = \{(u_1, u_2, I_1, I_2, \theta) \in R \times R \times R \times S|(u_1, u_2) = P_{2,3}, I_{11} < I < I_{12}, 0 \leq \theta_1 \leq 2\pi\}.$$

The latter four-dimensional equations on ${M_\varepsilon}^{\phi}$ are expressed as:

$$\dot{I}_1 = -\frac{1}{2}\mu_2 I_1 - \varepsilon\frac{1}{4}F_2\sin(\theta_1 + \phi), \tag{41}$$

$$I_1\dot{\theta}_1 = \frac{1}{4}\sigma_2 I_1 + c_8{I_1}^3 + c_9{u_1}^2 I_1 + c_{10}I_1{I_2}^2 - \frac{1}{4}\varepsilon F_2(\cos\theta_1 + \phi),$$

$$\dot{I}_2 = -\frac{1}{2}\mu_3 I_2 - \varepsilon\frac{1}{6}F_2\sin(\theta_2 + \phi),$$

$$I_2\dot{\theta}_2 = \frac{1}{6}\sigma_3 I_2 + c_{13}{I_2}^3 + c_5{u_1}^2 I_2 + c_{10}{I_1}^2 I_2 - \frac{1}{6}\varepsilon F_3\cos(\theta_2 + \phi).$$

Combining with the invariant manifold and the geometric structure of the five-dimensional stable manifold and unstable manifold, the influence of dissipative perturbations is analyzed.

Under dissipative perturbations, the invariant manifold M_0 becomes the invariant manifold $M_{0\varepsilon}$, $M_{0\varepsilon}$ is close enough to M_0.

$$M_0 \to M_{0\varepsilon} = \{(u_1, u_2, I, \theta) | (u_1, u_2) = P_1, I_{i1} < I < I_{i2}, 0 \le \theta_i \le 2\pi\} (\mathrm{i} = 1, 2). \tag{42}$$

Let $I_2 = I_{2r} \in U$, $I_2 \in [I_{2\theta} - \varepsilon, I_{2\theta} + \varepsilon] \subset [I_{21}, I_{22}]$, $\theta \in [0, 2\pi]$. To analyze the influence of the dissipative perturbations, introduce the transformation $I = I_r + \sqrt{\varepsilon} h$ and $\tau = \sqrt{\varepsilon} t$. The Hamilton system is expressed as:

$$\dot{h} = c_6 I_{1\theta} - \frac{1}{4} F_2 \sin(\theta_1 + \phi_0) + c_6 \sqrt{\varepsilon} h, \tag{43}$$

$$\dot{\theta}_1 = 2 I_{1\theta} c_8 h + \sqrt{\varepsilon} c_8 h^2 - \frac{\sqrt{\varepsilon} F_2}{4 I_{2\theta}} \cos(\theta_1 + \phi_0),$$

the Hamilton function is denoted as:

$$\Delta \hat{H}_D(h, \theta_1) = c_6 I_{1\theta} \theta_1 - c_8 I_{1\theta} h^2 + \frac{1}{4} F_2 \cos(\theta_1 + \phi_0). \tag{44}$$

When $\varepsilon = 0$, the fix points of the system (43) in the interval $\theta_1 \in (0, 2\pi)$ are given by:

$$Q_1 = (0, \theta_{1s}) = (0, \pi - \arcsin\frac{4 c_6 I_{1\theta}}{F_2}), Q_2 = (0, \theta_{1c}) = (0, \arcsin\frac{4 c_6 I_{1\theta}}{F_2}). \tag{45}$$

The characteristics of the Jacobi matrix of the unperturbed part in the system (43) at Q_1 and Q_2, which is

$$J = \begin{bmatrix} 0 & -\frac{1}{4} F_2 \cos\theta_1 \\ 2 c_8 I_{1\theta} & 0 \end{bmatrix}. \tag{46}$$

When $\frac{1}{2} c_8 F_2 I_{1\theta} \cos\theta_{1c} > 0$, the system (43) has two eigenvalues with opposite signs, the eigenvalues of Q_1 under the unperturbed system are $\lambda_{1,2} = \pm\sqrt{\frac{1}{2} c_8 F_2 I_{1\theta} \cos\arcsin\frac{c_6 I_{1\theta}}{F_2}}$, the eigenvalues of Q_2 are under the unperturbed system are $\lambda_{3,4} = \pm i\sqrt{\frac{1}{2} c_8 F_2 I_{1\theta} \cos\arcsin\frac{c_6 I_{1\theta}}{F_2}}$. Q_1 is a saddle point connected with the homoclinic orbit, Q_2 is the center point. The characteristics of the Jacobi matrix of the linear part of the system (43) under the dissipative perturbation ε, which is given by

$$J_\varepsilon = \begin{bmatrix} c_6 \sqrt{\varepsilon} & -\frac{1}{4} F_2 \cos\theta_1 \\ 2 c_8 I_{1\theta} & \frac{\sqrt{\varepsilon} F_2}{4 I_{1\theta}} \sin\theta_1 \end{bmatrix}. \tag{47}$$

The dynamical characteristics of the singular points Q_1 and Q_2 are uncovered. The eigenvalues of Q_1 are $\lambda^{\varepsilon}{}_{1,2} = c_6 \sqrt{\varepsilon} \pm \sqrt{\frac{1}{2} F_2 c_8 I_{1\theta} \cos\theta_{1s}}$, compared with the eigenvalues of the unperturbed system, Q_1 keeps hyperbolic properties, so the singular point Q_1 is still a saddle point with perturbation. The eigenvalues of Q_2 are $\lambda^{\varepsilon}{}_{3,4} = c_6 \sqrt{\varepsilon} \pm i\sqrt{\frac{1}{2} F_2 c_8 I_{1\theta} \cos\theta_{1s}}$, the center point Q_2 becomes a stable sink $Q_{\varepsilon 2}$ under small perturbations.

Considering the dissipation perturbation, the n-order energy difference function is:

$$\begin{aligned}
&\Delta^n H_D(u_1,u_2,I_1,I_2,\theta_1,\theta_2,\phi_0)\\
&=\hat{H}_D(h,\theta_1+n\Delta\theta)-\hat{H}_D(h,\theta_1)-n\int_A\left[\tfrac{d}{du_1}g^{u_1}(u_1,u_2,I,\theta)\tfrac{d}{du_2}g^{u_2}(u_1,u_2,I,\theta)\right]du_1du_2-n\int\limits_{\partial A_1}g^I d\theta\\
&=nc_6I_{1r}\Delta\theta_1+\tfrac{1}{4}F_2[\cos(\theta_1+\phi_0+n\Delta\theta_1)-\cos(\theta_1+\phi_0)]+\tfrac{16n\mu_1\varepsilon_1\Delta\theta_1}{3c_3\sqrt{\varepsilon_1}}+nc_{11}I_{2r}\Delta\theta_2.
\end{aligned} \tag{48}$$

$\hat{H}_D(h,\theta_1+N\Delta\theta_1)$ is the energy function of n pulses. $\hat{H}_D(h,\theta_1)$ represents the first pulse. $\Delta\theta$ is the phase shift. The expression of dissipation factor is

$$d=\frac{\mu_1}{F_2}=\frac{3c_3\sqrt{c_1}[\sqrt{F_2^2-16{c_6}^2{I_{1\theta}}^2}[1-\cos(n\Delta\theta_1+\phi_0)]+4c_6I_{1\theta}\sin(n\Delta\theta_1+\phi_0)]}{16n\varepsilon_1\Delta\theta_1F_2-6c_3\sqrt{c_1}I_{1\theta}\Delta\theta_2F_2}, \tag{49}$$

where d depicts the relationship between the dissipation factor and the external excitation. When the dissipative energy difference function satisfies the condition $\Delta^n\hat{H}_D(u_1,u_2,I_1,I_2,\theta_1,\theta_2,\phi_0)=0$ and $\alpha=\frac{n\Delta\theta_1}{2}+\theta_1+\phi_0$, the following equation can be obtained:

$$\sin\alpha=\sin\left(\frac{n\Delta\theta_1}{2}+\theta_1+\phi_0\right)=\frac{32n\mu_1\varepsilon_1\Delta\theta_1+6nc_3\sqrt{c_1}c_{11}I_{2\theta}\Delta\theta_2}{3F_2c_3\sqrt{c_1}\sin(\frac{n\Delta\theta_1}{2}+\phi_0)}. \tag{50}$$

According to Equation (49), due to $d<1$, it can be drawn that:

$$|n|<n_{\max}=\frac{3c_3\sqrt{c_1}[\sqrt{F_2^2-16{c_6}^2{I_{1\theta}}^2}[1-\cos(n\Delta\theta_1+\phi_0)]}{16n\varepsilon_1\Delta\theta_1F_2-6c_3\sqrt{c_1}I_{1\theta}\Delta\theta_2F_2}. \tag{51}$$

The upper bound on the maximum number of pulses $n_{\max}$ for multi-pulse chaotic motion is obtained. To compute the transversal zeros of the energy difference function, define a set containing the transversal zeros of the dissipative energy difference function as follows:

$$\hat{z}_{-1}^N\triangleq\left\{(h,\theta)\middle|\Delta^N\hat{H}_D(u_1,u_2,I_1,I_2,\theta_1,\theta_2,\phi_0)=0,D_\theta\middle|\Delta^N\hat{H}_D(u_1,u_2,I_1,I_2,\theta_1,\theta_2,\phi_0)\neq 0\right\}. \tag{52}$$

The transversal zeros of the dissipative energy difference function $\Delta^N\hat{H}_D(u_1,u_2,I_1,I_2,\theta_1,\theta_2,\phi_0)$ satisfy the condition:

$$\theta_1+\frac{n\Delta\theta_1}{2}+\phi_0=2n\pi+(-1)^m\alpha,\theta_1\in[-\frac{\pi}{2},\frac{3\pi}{2}]. \tag{53}$$

The following relationship is obtained as follows:

$$\alpha=\arcsin\left[\frac{32n\mu_1\varepsilon_1\Delta\theta_1+6nc_3\sqrt{c_1}c_{11}I_{2\theta}\Delta\theta_2}{3F_2c_3\sqrt{c_1}\sin(\frac{n\Delta\theta_1}{2}+\phi_0)}\right]. \tag{54}$$

When the condition $n\Delta\theta_1\neq 4k\pi, k=0,1,2\ldots$ is satisfied, two transversal zeros $\Delta^n\hat{H}_D(u_1,u_2,I_1,I_2,\theta_1,\theta_2,\phi_0)$ are denoted by:

$$\theta_{0,1}^{\pi}=\frac{3\pi}{2}-\left(\frac{n\Delta\theta_1}{2}-\alpha\right)\mathrm{mod}2\pi,\theta_{0,2}^{\pi}=\frac{3\pi}{2}-\left(\pi+\frac{n\Delta\theta_1}{2}-\alpha\right)\mathrm{mod}2\pi. \tag{55}$$

The transversal zeros satisfy the non-degenerate condition (53); it is verified that there exist non-degenerate zeros in the Hamilton function $\Delta\hat{H}_D(h,\theta_1)$ of the system. When $d\neq 0$, the center point Q_2 is the zero point of the energy difference function.

$$\begin{cases} n\Delta\theta_1 + \phi_0 \neq 2k\pi, k \in Z^+ \\ D_d \Delta \hat{H}_D(h, \theta_1, \phi_0) = D_d(\frac{1}{4}F_2(\cos(\theta_1 + n\Delta\theta_1 + \phi_0) - \cos(\theta_1 + \phi_0))) + \frac{16n\mu_1\varepsilon_1\Delta\theta_1}{3c_3\sqrt{c_1}} + nc_{11}I_{2r}\Delta\theta_2 \end{cases} \quad (56)$$

To verify the existence of multi-pulse chaotic motion in the system, it is necessary to examine the multi-pulse orbit from the slow manifold returns to the attraction domain of the focus. From the Hamilton function (44), the estimated domain of attraction of $\theta_{\min}$ can be obtained as:

$$c_6 I_{1\theta}\theta_{\min} + \frac{1}{4}F_2\cos(\theta_{\min} + \phi_0) = c_6 I_{1\theta}\theta_{1c} + \frac{1}{4}F_2\cos(\theta_{1c} + \phi_0). \quad (57)$$

Substituting the fixed point Q_2 into Equation (57), the estimated domain of attraction of $\theta_{\min}$ is given by:

$$\theta_{\min} + \frac{F_2}{4c_6 I_{1\theta}}\cos(\theta_{\min} + \phi_0) = \arccos\frac{4c_6 I_{1\theta}}{F_2} + k, \quad (58)$$

where k is a constant. Define an annulus A_ε near $I = I_{1\theta}$ as

$$A_\varepsilon = \left\{(u_1, u_2, I_1, I_2, \theta_1, \theta_2) \middle| u_1 = B, u_2 = 0, |I - I_i| < C\sqrt{\varepsilon}, \theta_i \in S^1, (i = 1, 2)\right\}. \quad (59)$$

the constant C ensures that the unperturbed orbit is always contained in the annulus domain.

The saddle point Q_1 and the center point Q_2 correspond to the energy function $\hat{H}_D(0, \theta_{1s})$ and $\hat{H}_D(0, \theta_{1c})$, respectively. In the interval (0,2π), the pulse jumps from the starting point Q_2 and returns to point Q. The energy function of Q is $\hat{H}_D(0, \theta_{1*})$. Since the distance between the center point and the falling point is larger than $2k\pi$, define the falling point $\theta_{1*} - 2k\pi$ as

$$\theta_{1*}^N = \theta_{1s} + [\theta_{1c} + N\Delta\theta_1 - \theta_{1s}]\mathrm{mod}2k\pi, \quad (60)$$

where $\theta_{1s} = \pi + \arcsin 2dI_{1\theta}$, $\theta_{1c} = -\arcsin 2dI_{1\theta}$.

The energy at the starting point is the largest. When the falling point keeps away from the start point, the energy gradually decreases. The minimum energy corresponds to the saddle point Q_1. When the energy of the falling point is larger than the saddle point, that is

$$\hat{H}_D(0, \theta_{1*}) > \hat{H}_D(0, \theta_{1s}). \quad (61)$$

The falling point finally comes back to the attraction domain of the sink. From the proof of the above process, it is known that there exists a Shilnikov multi-pulse chaotic motion in the six-dimensional non-autonomous system.

To verify the above theoretical analysis, numerical simulations and analysis are carried out based on the six-dimensional average Equation (2) in the Cartesian coordinate system. The parameters are chosen as $\mu_1 = \mu_2 = \mu_3 = \mu = 0.06$, $\sigma_1 = 0.12$, $\sigma_2 = 0.19$, $\sigma_3 = 3.12$, $\alpha_{14} = 1.24$, $\alpha_{21} = 0.9$, $\alpha_{25} = 3.9$, $\beta_{15} = 2.11$, $\beta_{20} = 7$, $\beta_{23} = 24$, $\beta_{24} = 2$, $\gamma_{16} = 2$, $\gamma_{20} = 5$, $\gamma_{22} = 2.5$, $\gamma_{24} = 2.3$, $F_1 = 9$, $F_2 = 90$. We choose F_3 as the primary variable. The initial condition of the selected system is chosen as $x_{10} = 0.44$, $x_{20} = 0.2$, $x_{30} = 0.35$, $x_{40} = 0.19$, $x_{50} = 0.01$, $x_{60} = 0.06$. The Runge–Kutta algorithm is taken advantage of by the numerical simulations.

Figure 13a–f show the waveform, phase portraits, spectrogram map, the Maximum Lyapunov exponent and Poincare maps for the system when $F_3 = 30$. When $F_3 = 40$, Figure 14 shows the corresponding numerical simulation results. It is concluded that chaos occurs in the six-dimensional non-autonomous system for the circular mesh antenna.

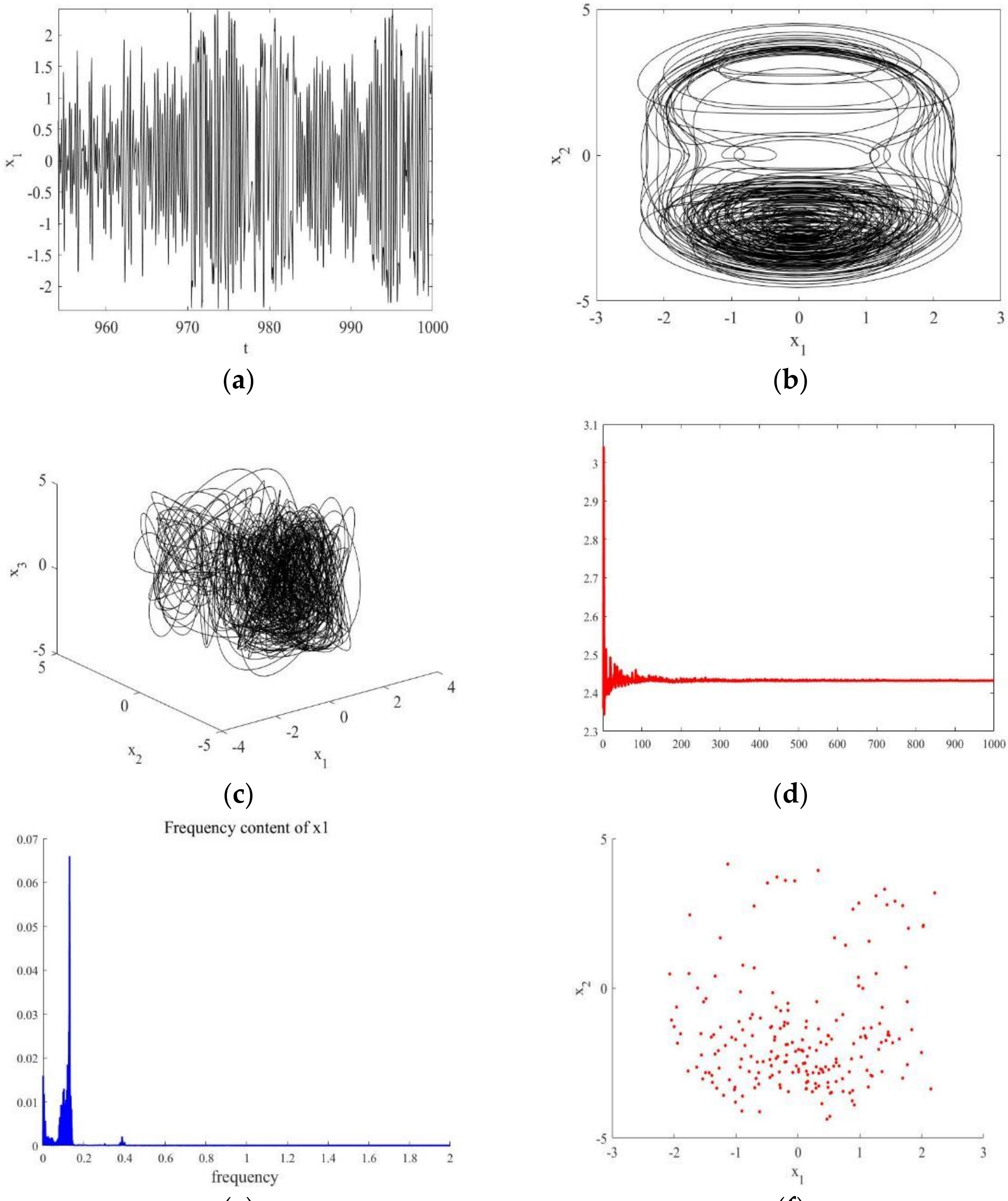

Figure 13. The trajectory under the condition $F_3 = 30$. (**a**) The waveform on the plane (t,x_1); (**b**) The phase portrait on the plane (x_1,x_2). (**c**) The phase portrait in the three-dimensional space (x_1,x_2,x_3). (**d**) The Maximum Lyapunov exponent plot of x_1. (**e**) The power spectrum of x_1. (**f**) The Poincare map on the plane (x_1,x_2).

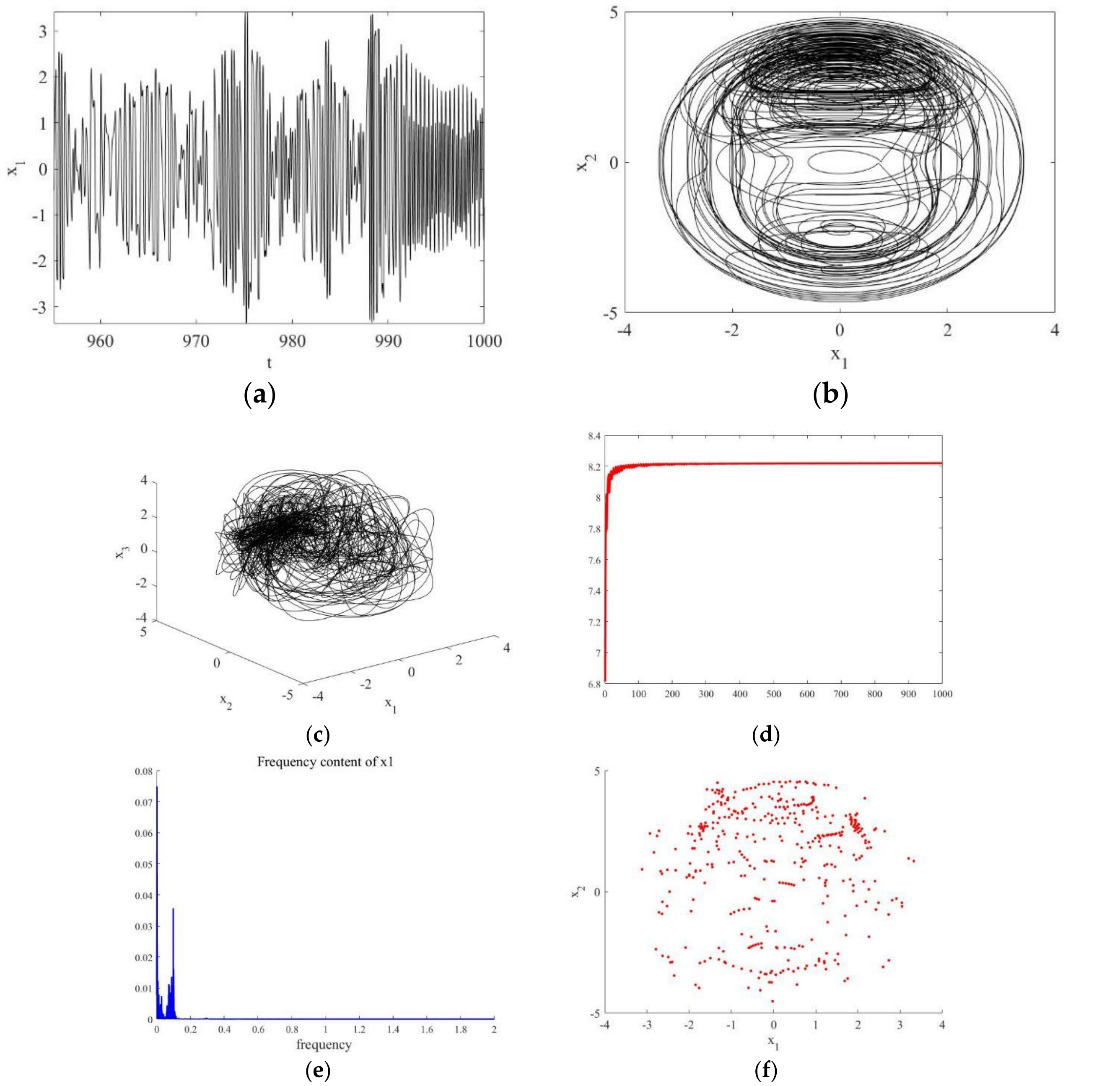

Figure 14. The trajectory under the condition $F_3 = 40$. (**a**) The waveform on the plane (t,x_1). (**b**) The phase portrait on the plane (x_1,x_2). (**c**) The phase portrait in the three-dimensional space (x_1,x_2,x_3). (**d**) The Maximum Lyapunov exponent plot of x_1. (**e**) The power spectrum of x_1. (**f**) The Poincare map on the plane (x_1,x_2).

5. Conclusions

The Smale horseshoe and multi-pulse chaotic motion of a six-dimensional non-autonomous system for the circular mesh antenna are verified. Through the construction of the Poincare map in the first two-dimensional system, the positional relationship and geometric structure between the fixed point and periodic orbits are obtained. For the latter four-dimensional system, the three-dimensional solid torus structure is mapped to the logarithmic spiral structure. There exists chaos in the sense of the Smale horseshoe. The Shilnikov multi-pulse chaotic motion of the six-dimensional non-autonomous system is verified by the extended energy phase method. From the analysis of the above two parts, the following conclusions can be drawn.

1. In the process of the Poincare map of the six-dimensional non-autonomous system, the map contains two expanding directions and one contracting direction in the cross-section. According to the topological horseshoe theory, there exists chaos in the sense of a Smale horseshoe.
2. Through the calculation of the energy difference function, the conditions for generating Shilnikov-type chaos in the six-dimensional non-autonomous systems are obtained in theory. When the orbit converges to the focus, the Shilnikov-type orbit jumps up again and repeats this motion in the six-dimensional phase space. The Shilnikov-type multi-pulse orbit with energy dissipation is formed.

Author Contributions: Conceptualization, Y.S. and J.L.; methodology, J.L.; software, J.L.; validation, J.L., Y.S. and J.Z.; formal analysis, Y.S.; investigation, Y.S.; resources, J.L.; data curation, J.L.; writing—original draft preparation, Y.S.; writing—review and editing, Y.S. and J.L.; visualization, A.W. and F.M.; supervision, J.Z.; project administration, Y.S.; funding acquisition, Y.S. All authors have read and agreed to the published version of the manuscript.

Funding: The authors gratefully acknowledge the support of the National Natural Science Foundation of China (Nos. 11902038, 12272057 and 12272058).

Conflicts of Interest: The authors declare that they have no known competing financial interests or personal relationship that could have appeared to influence the work reported in this paper.

References

1. Morterolle, S.; Maurin, B.; Dube, J.F.; Averseng, J.; Quirant, J. Modal behavior of a new large reflector conceptual design. *Aerosp. Sci. Technol.* **2015**, *42*, 74–79. [CrossRef]
2. Li, P.; Liu, C.; Tian, Q.; Hu, H.Y.; Song, Y.P. Dynamics of a deployable mesh reflector of satellite antenna: Form-finding and modal analysis. *J. Comput. Nonlinear Dyn.* **2016**, *11*, 041017-12. [CrossRef]
3. Nie, R.; He, B.; Zhang, L. Deployment dynamics modeling and analysis for mesh reflector antennas considering the motion feasibility. *Nonlinear Dyn.* **2018**, *91*, 549–564. [CrossRef]
4. Zhang, W.; Zheng, Y.; Liu, T.; Guo, X.Y. Multi-pulse jumping double-parameter chaotic dynamics of eccentric rotating ring truss antenna under combined parametric and external excitations. *Nonlinear Dyn.* **2019**, *98*, 761–800. [CrossRef]
5. Wang, Q.D.; Oksasoglu, A. Periodic occurrence of chaotic behavior of homoclinic tangles. *Phys. D* **2010**, *239*, 387–395. [CrossRef]
6. Wang, Q.D.; Oksasoglu, A. Dynamics of homoclinic tangles in periodically perturbed second-order equations. *J. Differ. Equ.* **2011**, *250*, 710–751. [CrossRef]
7. Hirsch, M.; Smale, S. Differential equations, dynamical systems and linear algebra. *Bull. Am. Math. Soc.* **1967**, *73*, 747–817.
8. Li, T.Y.; Yorke, J.A. Period three implies chaos. *Am. Math. Mon.* **1975**, *82*, 985–992. [CrossRef]
9. Poincaré, H. Mémoire sur les courbes définies par une équation differetielle (I). *J. Math.* **1881**, *7*, 375–422.
10. Poincaré, H. Mémoire sur les courbes définies par une équation differetielle (II). *J. Math.* **1882**, *8*, 251–296.
11. Landi, P.; Dercole, F. The social diversification of fashion. *J. Math. Sociol.* **2016**, *40*, 185–205. [CrossRef]
12. Guastello, S.J. Nonlinear dynamics in psychology. *Discrete Dyn. Nat. Soc.* **2001**, *6*, 11–29. [CrossRef]
13. Smith, B.W. Chaotic family dynamics. *Arch. Fam. Med.* **1994**, *3*, 8–123. [CrossRef] [PubMed]
14. Huang, L.Y.; Bae, Y. Periodic doubling and chaotic attractor in the love model with a Fourier series function as external force. *Int. J. Fuzzy Log. Intell. Syst.* **2017**, *17*, 17–25. [CrossRef]
15. Deng, W.; Liao, X.F. Complex Dynamics in a Love-Triangle Model with Single-Frequency and Multiple-Frequency External Forcing. *Int. J. Bifurcate. Chaos.* **2019**, *29*, 1950133. [CrossRef]
16. Huang, L.Y.; Bae, Y. Nonlinear Behavior in Romeo and Juliet's Love model Influenced by External Force with Fuzzy Membership Function. *Int. J. Fuzzy Syst.* **2017**, *16*, 64–71. [CrossRef]
17. Huang, L.Y.; Bae, Y. Analysis of Chaotic Behavior in a Novel Extended Love Model Considering Positive and Negative External Environment. *Entropy* **2018**, *20*, 365. [CrossRef]
18. Wang, Z.; Veeman, D.; Zhang, M. A symmetric oscillator with multi-stability and chaotic dynamics: Bifurcations, circuit implementation, and impulsive control. *Eur. Phys. J. Spec. Top.* **2021**, *231*, 2153–2161. [CrossRef]
19. Zhang, W.; Wu, Q.L.; Zhang, Y.F.; Zheng, Y. Coexistence of bistable multi-pulse chaotic motions with large amplitude vibrations in buckled sandwich plate under transverse and in-plane excitations. *Chaos Interdiscip. J. Nonlinear Sci.* **2020**, *30*, 043121. [CrossRef]
20. Zhang, L.P.; Liu, Y.; Wei, Z.C. Hidden attractors in a class of two-dimensional rational memristive maps with no fixed points. *Eur. Phys. J. Spec. Top.* **2022**, *231*, 2173–2182. [CrossRef]
21. Wen, S.F.; Qin, H.; Shen, Y.J. Chaos threshold analysis of Duffing oscillator with fractional-order delayed feedback control. *Eur. Phys. J. Spec. Top.* **2022**, *231*, 2183–2197. [CrossRef]
22. Tian, H.G.; Wang, Z.; Zhang, H. Dynamical analysis and fixed-time synchronization of a chaotic system with hidden attractor and a line equilibrium. *Eur. Phys. J. Spec. Top.* **2022**, *231*, 2455–2466. [CrossRef]

23. Huan, S.; Li, Q.; Yang, X.S. Chaos in three-dimensional hybrid systems and design of chaos generators. *Nonlinear Dyn.* **2012**, *69*, 1915–1927. [CrossRef]
24. Li, J.; Tomsovic, S. Homoclinic orbit expansion of arbitrary trajectories in chaotic systems: Classical action function and itsmemory. *arXiv* **2020**, arXiv:2009.12224.
25. Shilnikov, L.P. A case of the existence of a countable number of periodic motions. *Sov. Math. Dokl.* **1965**, *6*, 163–166.
26. Shilnikov, L.P.; Shilnikov, A.L.; Turaev, D.V.; Chua, L.O. *Methods of Qualitative Theory in Nonlinear Dynamics*; World Scientific Publishing: Singapore, 1998.
27. Liu, X.L.; Han, M.A. Bifurcation of periodic solutions and invariant tori for a four-dimensional system. *Nonlinear Dyn.* **2009**, *57*, 75–83. [CrossRef]
28. Camassa, R.; Kovacic, G.; Tin, S.K. A Melnikov method for homoclinic orbits with many pulses. *Arch. Ration. Mech. Anal.* **1998**, *143*, 105–193. [CrossRef]
29. Kaper, T.J.; Kovacic, G. Multi-bump orbits homoclinic to resonance bands. *Trans. Am. Math. Soc.* **1996**, *348*, 3835–3887. [CrossRef]
30. Zhou, S.; Yu, T.J.; Yang, X.D.; Zhang, W. Global dynamics of pipes conveying pulsating fluid in the supercritical regime. *Int. J. of Appl. Mech.* **2017**, *9*, 1750029. [CrossRef]
31. Zhang, W.; Hao, W.L. Multi-pulse chaotic dynamics of six-dimensional non-autonomous nonlinear system for a composite laminated piezoelectric rectangular plate. *Nonlinear Dyn.* **2013**, *73*, 1005–1033. [CrossRef]
32. Zhang, M.; Chen, F.Q.; Li, F. Multi-pulse orbits and chaotic dynamics of a symmetric cross-ply composite laminated cantilever rectangular plate. *Nonlinear Dyn.* **2016**, *83*, 253–267. [CrossRef]
33. Wu, Q.L.; Zhang, W.; Dowell, E.H. Detecting multi-pulse chaotic dynamics of high-dimensional non-autonomous nonlinear system for circular mesh antenna. *Int. J. Nonlin. Mesh.* **2018**, *102*, 25–40. [CrossRef]
34. Zhang, W.; Gao, M.J.; Yao, M.H. Global analysis and chaotic dynamics of six-dimensional nonlinear system for an axially moving viscoelastic belt. *Int. J. Mod. Phys. B.* **2011**, *25*, 2299–2322. [CrossRef]
35. Chen, F.J.; Wang, Q.D. High order Melnikov method fortime-periodic equations. *Adv. Nonlinear Stud.* **2017**, *17*, 793–818. [CrossRef]
36. Chen, F.J.; Wang, Q.D. High order Melnikov method: Theory and application. *J. Differ. Equ.* **2019**, *267*, 1095–1128. [CrossRef]
37. Yu, T.J.; Zhou, S.; Zhang, W. Multi-pulse chaotic dynamics of an unbalanced Jeffcott rotor with gravity effect. *Nonlinear Dyn.* **2017**, *87*, 647–664. [CrossRef]
38. Sun, Y.; Zhang, W.; Yao, M.H. Multi-pulse chaotic dynamics and global dynamics analysis of circular mesh antenna with three-degree-of-freedom system. *Eur. Phys. J. Spec. Top.* **2021**, *231*, 2307–2324. [CrossRef]
39. Chertovskih, R.; Gama, S.; Podvigina, O.; Zheligovsky, V. Dependence of magnetic field generation by thermal convection on therotation rate: A case study. *Phys. D.* **2010**, *239*, 1188–1209. [CrossRef]
40. Cao, Y.; Chung, K.W.; Xu, J. A novel construction of homoclinic and heteroclinic orbits in nonlinear oscillators by a perturbation-incremental method. *Nonlinear Dyn.* **2011**, *64*, 221–236. [CrossRef]
41. Wiggins, S. *Global Bifurcations and Chaos: Analytical Methods*; Springer: New York, NY, USA, 1988; pp. 334–474.